Research in Astronomy and Astrophysics, 24:065014 (21pp), 2024 June https://doi.org/10.1088/1674-4527/ad420f

Isochrone Fitting of Galactic Globular Clusters—VI. High-latitude Clusters NGC 5024 (M53), NGC 5053, NGC 5272 (M3), NGC 5466, and NGC 7099 (M30)

G. A. Gontcharov[1], S. S. Savchenko[1,2,3], A. A. Marchuk[1,2], C. J. Bonatto[4], O. S. Ryutina[2], M. Yu. Khovritchev[1,2], V. B. Il'in[1,2,5], A. V. Mosenkov[6], D. M. Poliakov[1], and A. A. Smirnov[1]

[1] Central (Pulkovo) Astronomical Observatory, Russian Academy of Sciences, Pulkovskoye chaussee 65/1, St. Petersburg 196140, Russia; georgegontcharov@yahoo.com
[2] Saint Petersburg State University, Universitetskij pr. 28, St. Petersburg 198504, Russia
[3] Special Astrophysical Observatory, Russian Academy of Sciences, 369167 Nizhnij Arkhyz, Russia
[4] Departamento de Astronomia, Instituto de Física, UFRGS, Av. Bento Gonçalves, 9500, Porto Alegre, RS, Brazil
[5] Saint Petersburg University of Aerospace Instrumentation, Bol. Morskaya ul. 67A, St. Petersburg 190000, Russia
[6] Department of Physics and Astronomy, Brigham Young University, N283 ESC, Provo, UT 84602, USA
Received 2024 February 7; revised 2024 April 5; accepted 2024 April 22; published 2024 May 29

Abstract

We fit various color–magnitude diagrams (CMDs) of the high-latitude Galactic globular clusters NGC 5024 (M53), NGC 5053, NGC 5272 (M3), NGC 5466, and NGC 7099 (M30) by isochrones from the Dartmouth Stellar Evolution Database and Bag of Stellar Tracks and Isochrones for α–enrichment $[\alpha/\mathrm{Fe}] = +0.4$. For the CMDs, we use data sets from Hubble Space Telescope, Gaia, and other sources utilizing, at least, 25 photometric filters for each cluster. We obtain the following characteristics with their statistical uncertainties for NGC 5024, NGC 5053, NGC 5272, NGC 5466, and NGC 7099, respectively: metallicities $[\mathrm{Fe/H}] = -1.93 \pm 0.02$, -2.08 ± 0.03, -1.60 ± 0.02, -1.95 ± 0.02, and -2.07 ± 0.04 dex with their systematic uncertainty 0.1 dex; ages 13.00 ± 0.11, 12.70 ± 0.11, 11.63 ± 0.07, 12.15 ± 0.11, and 12.80 ± 0.17 Gyr with their systematic uncertainty 0.8 Gyr; distances (systematic uncertainty added) $18.22 \pm 0.06 \pm 0.60$, $16.99 \pm 0.06 \pm 0.56$, $10.08 \pm 0.04 \pm 0.33$, $15.59 \pm 0.03 \pm 0.51$, and $8.29 \pm 0.03 \pm 0.27$ kpc; reddenings $E(B-V) = 0.023 \pm 0.004$, 0.017 ± 0.004, 0.023 ± 0.004, 0.023 ± 0.003, and 0.045 ± 0.002 mag with their systematic uncertainty 0.01 mag; extinctions $A_V = 0.08 \pm 0.01$, 0.06 ± 0.01, 0.08 ± 0.01, 0.08 ± 0.01, and 0.16 ± 0.01 mag with their systematic uncertainty 0.03 mag, which suggest the total Galactic extinction $A_V = 0.08$ across the whole Galactic dust to extragalactic objects at the North Galactic Pole. The horizontal branch morphology difference of these clusters is explained by their different metallicity, age, mass-loss efficiency, and loss of low-mass members in the evolution of the core-collapse cluster NGC 7099 and loose clusters NGC 5053 and NGC 5466.

Key words: (stars:) Hertzsprung-Russell and C-M diagrams – (ISM:) dust – extinction – (Galaxy:) globular clusters: general – (Galaxy:) globular clusters: individual (NGC 5024, NGC 5053, NGC 5272, NGC 5466, NGC 7099)

1. Introduction

In Gontcharov et al. (2019, hereafter Paper I), Gontcharov et al. (2020, hereafter Paper II), Gontcharov et al. (2021, hereafter Paper III), Gontcharov et al. (2023b, hereafter Paper IV), and Gontcharov et al. (2023c, hereafter Paper V) we estimated important parameters (interstellar extinction in many filters, metallicity [Fe/H], age, and distance R from the Sun) for several Galactic globular clusters (GCs) via fitting their color–magnitude diagrams (CMDs) by theoretical isochrones based on stellar evolution models. Each CMD can provide us with independent estimates of [Fe/H], age, R, and reddening corresponding to the color of this CMD. The novelty of our results is due to recent appearances and improvements for models/isochrones and photometric data sets of individual cluster members in ultraviolet (UV), optical, and infrared (IR) bands, with accurate selection of the members by use of the precise parallaxes and proper motions (PMs) from the Hubble Space Telescope (HST; Libralato et al. 2022) and Gaia Data Release 3 (DR3; Gaia Collaboration et al. 2023). Both the recent data sets and isochrones successfully reproduce the main stages of stellar evolution, namely the main sequence (MS), turn-off (TO), subgiant branch (SGB), red giant branch (RGB), horizontal branch (HB), and asymptotic giant branch (AGB).

In this paper, we fit five high-latitude clusters: NGC 5024 (Messier 53, M53), NGC 5053, NGC 5272 (Messier 3, M3), NGC 5466, and NGC 7099 (Messier 30, M30). Some properties of these clusters are presented in Table 1. It shows

Table 1
Some Properties of the Clusters under Consideration

Property	NGC 5024	NGC 5053	NGC 5272	NGC 5466	NGC 7099
R.A. J2000 (h m s) from Goldsbury et al. (2010)	13 12 55	13 16 27	13 42 12	14 05 27	21 40 22
Decl. J2000 (° ′ ″) from Goldsbury et al. (2010)	+18 10 05	+17 42 01	+28 22 38	+28 32 04	−23 10 48
Galactic longitude (°) from Goldsbury et al. (2010)	332.9624	335.6983	42.2164	42.1499	27.1791
Galactic latitude (°) from Goldsbury et al. (2010)	+79.7641	+78.9461	+78.7069	+73.5923	−46.8354
Angular radius (arcmin) from Bica et al. (2019)	10.0	5.0	13.0	5.5	9.0
Tidal radius (arcmin) from Hunt & Reffert (2023)	6.8	4.5	8.6	6.4	8.7
Tidal radius (arcmin) from BV21	34.0	18.0	43.7	16.4	28.9
Truncation radius (arcmin) from this study	14.5	10.0	23.0	17.0	12.5
Core density (solar mass per cubic pc) from BV21	1259	3	6026	8	5 495 409
r_t/r_c from BV21	98	10	132	12	791
$\Delta(V-I)$ from Dotter et al. (2010)	0.851 ± 0.010	0.782 ± 0.041	0.736 ± 0.014	0.721 ± 0.025	0.872 ± 0.006
$\tau_{\rm HB}$ index from Torelli et al. (2019)	6.67 ± 0.16	4.35 ± 0.11	4.13 ± 0.05	5.02 ± 0.10	6.40 ± 0.20
HB type from Torelli et al. (2019)	$+0.89 \pm 0.06$	$+0.46 \pm 0.12$	$+0.21 \pm 0.02$	$+0.62 \pm 0.11$	$+0.90 \pm 0.10$
HB type from Arellano Ferro (2024)	+0.81	+0.50	+0.08	+0.58	+0.89
Mean HB type from this study	$+0.83 \pm 0.02$	$+0.74 \pm 0.17$	$+0.10 \pm 0.03$	$+0.62 \pm 0.08$	$+0.83 \pm 0.09$
R (kpc) from Harris (1996), 2010 revision[a]	17.9	17.4	10.2	16.0	8.1
R (kpc) from BV21	18.50 ± 0.18	17.54 ± 0.23	10.175 ± 0.082	16.12 ± 0.16	8.458 ± 0.090
R (kpc) from Arellano Ferro (2024)	18.0 ± 0.4	16.7 ± 0.4	10.0 ± 0.4	16.0 ± 0.6	8.1
R (kpc) from Hunt & Reffert (2023)	14.42 ± 0.34	19.21 ± 1.48	9.69 ± 0.09	17.67 ± 0.73	7.83 ± 0.12
[Fe/H] from Carretta et al. (2009)	-2.06 ± 0.09	-2.30 ± 0.08	-1.50 ± 0.05	-2.31 ± 0.09	-2.33 ± 0.02
[Fe/H] from Mészáros et al. (2020)	-1.89 ± 0.11	-2.06 ± 0.11	-1.39 ± 0.13	-1.83 ± 0.11	
Spectroscopic [Fe/H] from Jurcsik & Hajdu (2023)	-2.03 ± 0.04	-2.21 ± 0.03	-1.47 ± 0.02	-1.92 ± 0.05	-2.32 ± 0.10
Photometric [Fe/H] from Jurcsik & Hajdu (2023)	-1.87 ± 0.02	-2.01 ± 0.03	-1.48 ± 0.02	-1.98 ± 0.02	-2.18 ± 0.05
[Fe/H] from Arellano Ferro (2024)	-1.85 ± 0.13	-2.05 ± 0.18	-1.57 ± 0.14	-1.89 ± 0.21	−2.14
$\delta Y_{2G,1G}$ from Milone et al. (2018)	0.013 ± 0.007	-0.002 ± 0.013	0.016 ± 0.005	0.002 ± 0.017	0.015 ± 0.010
Age (Gyr) from Dotter et al. (2010)	13.25 ± 0.50	13.50 ± 0.75	12.50 ± 0.50	13.00 ± 0.75	13.25 ± 1.00
Age (Gyr) from Forbes & Bridges (2010)	12.67 ± 0.64	12.29 ± 0.51	11.39 ± 0.51	13.57 ± 0.64	12.93 ± 0.64
Age (Gyr) from VandenBerg et al. (2013)	12.25 ± 0.25	12.25 ± 0.38	11.75 ± 0.25	12.50 ± 0.25	13.00 ± 0.25
Age (Gyr) from Valcin et al. (2020)	$13.31^{+0.66}_{-0.57}$	$13.84^{+0.50}_{-0.58}$	$12.60^{+0.66}_{-0.66}$	$12.31^{+0.60}_{-0.40}$	$12.82^{+0.33}_{-0.50}$
$\overline{\Delta E(B-V)}$ (mag) from BCK13	0.030 ± 0.009	0.029 ± 0.011	0.031 ± 0.009	0.024 ± 0.009	0.030 ± 0.010
$\Delta E(B-V)_{\rm max}$ (mag) from BCK13	0.068	0.058	0.063	0.048	0.064
$E(B-V)$ (mag) from Harris (1996), 2010 revision	0.02	0.01	0.01	0.00	0.03
$E(B-V)$ (mag) from SFD98	0.02	0.02	0.01	0.02	0.05
$E(B-V)$ (mag) from Schlafly & Finkbeiner (2011)	0.02	0.01	0.01	0.01	0.04
$E(B-V)$ (mag) from Meisner & Finkbeiner (2015)	0.02	0.02	0.02	0.02	0.06
$E(B-V)$ (mag) from Lallement et al. (2019)	0.01	0.01	0.01	0.01	0.02
$E(B-V)$ (mag) from Green et al. (2019)	0.02	0.01	0.07	0.03	0.06
$E(B-V)$ (mag) from Gontcharov et al. (2023a)	0.04	0.05	0.02	0.05	0.07

Note. r_t/r_c is the ratio of tidal and core radii, $\Delta(V-I)$ is the median color difference between the HB and RGB from Dotter et al. (2010), R is the distance from the Sun, $\delta Y_{2G,1G}$ is the average helium difference between the second and first stellar generations, and $\overline{\Delta E(B-V)}$ and $\Delta E(B-V)_{\rm max}$ are the mean and maximum DR, respectively. We use the R and [Fe/H] estimates of Arellano Ferro (2024) for the RRc variables, with the [Fe/H] estimates being on the [Fe/H] scale of Carretta et al. (2009).

[a] The commonly used database of GCs by Harris (1996) (https://www.physics.mcmaster.ca/~harris/mwgc.dat), 2010 revision.

that tidal radius, metallicity, distance, and age of these clusters are quite uncertain and, hence, should be clarified. This uncertainty is evident from all previous studies [see a list of them in (Baumgardt & Vasiliev 2021, hereafter BV21)]. Some previous studies with mutual estimates of several parameters are presented in Table 2. The same method of isochrone fitting, even when applied to the same data sets for decades, has yielded dissimilar estimates. This inconsistency can be attributed to significant reasons: the large uncertainty in the photometry used, which is at a level of 0.1 mag, and the contamination of the data by non-members. Both issues can be addressed with recent data sets. These data sets offer photometry with precision to a few hundredths of a magnitude and are complemented by highly accurate PMs and parallaxes. This study employs such advanced data sets to overcome the aforementioned challenges.

The clusters under consideration have a lot of estimates of metallicity [Fe/H]. Four of the clusters with a low metallicity [Fe/H] ≈ -2 (i.e., all but NGC 5272) are among the most metal-poor GCs and, hence, they are our first test of the

Table 2
Some Previous Mutual Estimates of the Parameters of the Clusters under Consideration

Study	[Fe/H]	Age	R	$E(B-V)$ or A_V
		NGC 5024		
Dotter et al. (2010)	−2.00	13.25 ± 0.50	18.95	$E(B-V)=0.023$
		NGC 5053		
Dotter et al. (2010)	−2.40	13.50 ± 0.75	18.04	$E(B-V)=0.021$
Arellano Ferro et al. (2010)	−1.97 ± 0.16	12.5 ± 2.0	16.7 ± 0.3	
Paust et al. (2010)	−1.99	12.0	17.27	$E(B-V)=0.04$
Nikitha et al. (2022)	−1.9	12.5 ± 2.0	17.06	
		NGC 5272		
Dotter et al. (2010)	−1.60	12.50 ± 0.50	10.22	$E(B-V)=0.018$
Paust et al. (2010)	−1.57	12.0	10.17	$E(B-V)=0.04$
Stenning et al. (2016)	−1.465 ± 0.003	11.80 ± 0.06	10.20 ± 0.03	$A_V=0.075\pm0.002$
Denissenkov et al. (2017)	−1.55	12.6	9.91	$E(B-V)=0.013$
Preet Kaur & Joshi (2022)	−1.57	11.56	10.47	$E(B-V)=0.015$
		NGC 5466		
Dotter et al. (2010)	−2.10	13.00 ± 0.75	16.43	$E(B-V)=0.023$
Paust et al. (2010)	−2.22	12.0	16.28	$E(B-V)=0.05$
		NGC 7099		
Dotter et al. (2010)	−2.40	13.25 ± 1.00	8.80	$E(B-V)=0.053$
Paust et al. (2010)	−2.12	13.0	8.14	$E(B-V)=0.07$
Kains et al. (2013)	−2.06 ± 0.12	13.0 ± 1.0	8.33 ± 0.45	

Note. We average results obtained by different methods inside each study. Age is in Gyr, R is in kpc.

models/isochrones in such a low-metallicity regime. Table 1 shows examples of large discrepancies between spectroscopic and photometric estimates of [Fe/H], between various spectroscopic estimates themselves. A detailed study of this issue is presented by Mucciarelli & Bonifacio (2020). They argue in favor of photometrically and against spectroscopically derived [Fe/H] for low-metallicity GCs. Since the slopes of the RGB and faint MS are sensitive to [Fe/H], our isochrone fitting of CMDs with well-populated bright RGB or faint MS can provide new independent [Fe/H] estimates for these clusters. Note that we estimate [Fe/H] separately for each model. As noted in Paper V, crowding or poor astrometry at the cluster centers, saturation and completeness effects, photometric errors and helium abundance Y uncertainty may result in an uncertainty of about 0.2 dex in our [Fe/H] estimate obtained from any pair of one CMD and one model.

Uncertain [Fe/H], age, and distance of the four low-metallicity clusters do not allow one to make a final conclusion about their similarity or origin. Yoon & Lee (2002) find that these clusters display a planar alignment of their positions and orbits in the outer halo, which, being combined with their other properties, suggests their captured origin from a satellite galaxy. This is supported by Chun et al. (2020) and should be confirmed, at least for NGC 5024 and NGC 5053, whose proximity in space to each other cannot be accidental.

Even foreground reddening of all the clusters [e.g., reddening $E(B-V)$], certainly being very low, is not well defined, as suggested by a noticeable differential reddening (DR) found by Bonatto et al. (2013, hereafter BCK13) and presented in Table 1. In this context, these clusters are interesting targets for further research. In particular, these clusters can be probes of total Galactic extinction at high latitudes, while very low reddening and extinction make them a test of the models/isochrones in such a low-extinction regime, where they should not predict an unreal negative extinction/reddening.

Table 1 also shows that these clusters differ in the HB morphology indexes: $\Delta(V-I)$ defined by Dotter et al. (2010), $\tau_{\rm HB}$ defined by Torelli et al. (2019), and HB type[7] calculated by Torelli et al. (2019) and Arellano Ferro (2024), albeit similar, at least, for NGC 5024 and NGC 7099. This forces us to analyze the HB morphology difference of the clusters in Section 3.1. This difference may be related to the difference in structural parameters of these clusters presented in Table 1: e.g., a core-collapse NGC 7099 with a compact core that differs strikingly from loose NGC 5466 and NGC 5053 in terms of core density and ratio r_t/r_c of tidal and core radius.

The clusters under consideration have, at least, two stellar generations (Milone et al. 2017) with a similar α–enrichment $[\alpha/{\rm Fe}]\approx0.4$ (Carretta et al. 2010; Kacharov et al. 2015; Boberg et al. 2015, 2016; Masseron et al. 2019; Chun et al.

[7] The HB type is defined as $(N_B-N_R)/(N_B+N_V+N_R)$, where N_B, N_V, and N_R are the number of stars that lie blueward of the instability strip, the number of RR Lyrae variables, and the number of stars that lie redward of the instability strip, respectively (Lee et al. 1994).

2020), but slightly different helium enrichment, as seen from Table 1. As in our previous studies, we check that this helium enrichment is mild in order to fit a cluster dominant generation or a mix of generations with reliable results. Specifically, we fit isochrones to all considered CMDs using a reasonable grid of helium abundance Y, metallicity [Fe/H], distance, reddening, and age. We use the α–enhanced theoretical models of stellar evolution and corresponding isochrones from Dartmouth Stellar Evolution Database (DSED, Dotter et al. 2007, 2008)[8] and a Bag of Stellar Tracks and Isochrones (BaSTI, Hidalgo et al. 2018; Pietrinferni et al. 2021),[9] which turned out to be suitable for such a fitting in our previous studies. Also, we use the BaSTI extended set of zero-age horizontal branch (ZAHB) models with a stochastic mass loss between the MS and HB. For control of our DSED fitting, we rely on the DSED HB and AGB isochrones, which exist for some filters. The DSED isochrones for $Y = 0.25$ and 0.33 and BaSTI isochrones for $Y = 0.25$ and $Y = 0.275$ are utilized to interpolate or extrapolate isochrones for other Y. Such interpolation produces a negligible uncertainty less than 0.01 mag in any CMD, since the initial isochrones are close to each other and they are presented by the same evolutionary points.

Figure 1 presents an example of CMDs where the BaSTI isochrones with different Y are drawn (together with the DSED isochrones for $Y = 0.25$). Other CMDs demonstrate a similar pattern, but we do not show the BaSTI isochrones with $Y = 0.275$ in Figures 2–4 for clarity. A noticeable separation of the isochrones with $Y = 0.25$ and 0.275 at the HB and AGB allows us to conclude that most stars fit $Y = 0.25$. This agrees, for example, with a robust estimate $Y = 0.252 \pm 0.003$ for NGC 7099 (Mucciarelli et al. 2014). We adopt $Y = 0.25$ for all domains of our CMDs, except the HB bluer than the RR Lyrae gap for NGC 5272 and the faint RGB of all the clusters, for which we adopt $Y = 0.275$.

NGC 5272 is the only cluster under consideration with a significant magnitude difference between the red and blue HB stars, as seen in the NGC 5272 CMDs in Figures 1–4. We explain this difference by the different helium enrichment in agreement with findings of Dalessandro et al. (2013), Valcarce et al. (2016). However, our CMDs in Figures 1–4 show that such an enrichment has little, if any, impact on the color of the blue HB stars and, hence, cannot explain any noticeable HB morphology difference. In particular, it cannot explain the famous HB morphology difference between NGC 6205 (M13) with its long HB blue tail (see Paper II) and NGC 5272 without such a tail (see Catelan 2009).

Since this is the sixth paper in this series, many details of our analysis can be found in our previous papers. We refer the reader to those papers, especially to the last ones, since we believe that our studies become more refined from paper to paper.

[8] http://stellar.dartmouth.edu/models/

[9] http://basti-iac.oa-abruzzo.inaf.it/index.html

This paper is organized as follows. In Section 2, we present the data sets used. The results of our isochrone fitting are given and discussed in Section 3. We summarize our main findings and conclusions in Section 4.

2. Data Sets

For all the clusters, there are cognate data sets, which are obtained with the same telescope and/or processed within the same pipeline:

1. the HST Wide Field Camera 3 (WFC3) UV Legacy Survey of Galactic Globular Clusters (the F275W, F336W, and F438W filters) and the Wide Field Channel of the Advanced Camera for Surveys (ACS; the F606W and F814W filters) survey of Galactic GCs (Piotto et al. 2015), (Nardiello et al. 2018, hereafter NLP18)[10] (74 205, 10 685, 71 049, 15 139, and 34 662 cluster members are used in NGC 5024, NGC 5053, NGC 5272, NGC 5466, and NGC 7099, respectively) with additional photometry in the ACS F435W or F555W filters for 52 542 members of NGC 5272 (Libralato et al. 2022),[11]
2. Gaia DR3 photometry in the G, G_{BP} and G_{RP} filters (Riello et al. 2021): 2812, 1124, 9281, 1863, and 3307 cluster members are used for NGC 5024, NGC 5053, NGC 5272, NGC 5466, and NGC 7099, respectively,[12]
3. *UBVRI* photometry from various ground-based telescopes processed by Stetson et al. (2019, hereafter SPZ19):[13] 4467, 1458, 10 192, 2156, and 3186 cluster members, common in SPZ19 and Gaia DR3 (hereafter Gaia-induced members), are used for NGC 5024, NGC 5053, NGC 5272, NGC 5466, and NGC 7099, respectively, or 9713 and 15 078 stars of the original SPZ19 data sets are used for NGC 5053 and NGC 5466, respectively,[14]
4. Panoramic Survey Telescope and Rapid Response System Data Release I (Pan-STARRS, PS1) photometry in the g_{PS1}, r_{PS1}, i_{PS1}, z_{PS1}, and y_{PS1} filters (Chambers et al. 2016): 3248, 1307, 9864, 2174, and 3426 Gaia-induced members are used for NGC 5024, NGC 5053, NGC 5272, NGC 5466, and NGC 7099, respectively,[15]

The following data sets exist for some but not all the clusters:

[10] http://groups.dfa.unipd.it/ESPG/treasury.php

[11] https://archive.stsci.edu/hlsp/hacks

[12] The DSED isochrones for Gaia DR2 are equally suitable for DR3.

[13] http://cdsarc.u-strasbg.fr/viz-bin/cat/J/MNRAS/485/3042 with recent updates at https://www.canfar.net/storage/vault/list/STETSON/homogeneous/Latest_photometry_for_targets_with_at_least_BVI

[14] We use the SPZ19 and other original data sets for NGC 5053 and NGC 5466 as an alternative of Gaia-induced members from these data sets, since these distant and loose clusters have not so many Gaia DR3 stars, whereas, on the other hand, these clusters have few contaminants due to their high latitude (see NGC 5053 CMD in Figure 3) and, hence, the original data sets, without any member selection, provide a reliable isochrone fitting with the same results as for their Gaia-induced members.

[15] NGC 7099 is not far from the decl. limit of PS1 at about −30° and, hence, it demonstrates less accurate PS1 photometry.

5 Sloan Digital Sky Survey (SDSS) photometry in the u_{SDSS}, g_{SDSS}, r_{SDSS}, i_{SDSS}, and z_{SDSS} filters (An et al. 2008):[16] 3365, 1308, 9336, and 3545 Gaia-induced members of NGC 5024, NGC 5053, NGC 5272, and NGC 5466, respectively, or 4162 and 8530 stars of the original SDSS data set for NGC 5053 and NGC 5466, respectively,

6 SkyMapper Southern Sky Survey DR3 (SMSS, SMSS DR3) photometry in the g_{SMSS}, r_{SMSS}, i_{SMSS}, and z_{SMSS} filters (Onken et al. 2019),[17] for 1729 Gaia-induced members of NGC 7099,

7 Photometry in the F439W and F555W filters from the HST Wide Field and Planetary Camera 2 (WFPC2) (Piotto et al. 2002)[18] for 9526 and 4698 stars in NGC 5024 and NGC 7099, respectively,

8 Wide-field Infrared Survey Explorer (WISE; Wright et al. 2010) photometry in the *W*1 filter from the unWISE catalog (Schlafly et al. 2019)[19] for 902 and 444 Gaia-induced members of NGC 5272 and NGC 7099, respectively (the unWISE photometry for the remaining, more distant clusters is not deep enough for reliable results),

9 *BV* photometry of 23431 stars from the original data set of Rey et al. (1998)[20] or its 616 Gaia-induced members of NGC 5024 obtained with the University of Hawaii 2.2 m telescope, Mauna Kea,

10 *VI* photometry of 539 Gaia-induced members of NGC 5053 obtained with the 0.9 m telescope at Kitt Peak National Observatory (KPNO) and the 1.2 m telescope at Whipple Observatory, Mt. Hopkins, Arizona (Sarajedini & Milone 1995),[21]

11 Strömgren *uvby* photometry of 16403 stars of the original data set of Grundahl et al. (1999, hereafter GCL99) or its 666 Gaia-induced members of NGC 5272 obtained with the Nordic Optical Telescope (NOT), La Palma,

12 Strömgren *uvby* photometry of 4703 Gaia-induced members of NGC 5272 obtained with the Isaac Newton Telescope Wide Field Camera (INT-WFC), La Palma (Massari et al. 2016),[22]

13 *BV* photometry of 10 540 stars of the original data set of Sandage (1953) and Buonanno et al. (1994)[23] or its 2194 Gaia-induced members of NGC 5272 obtained from

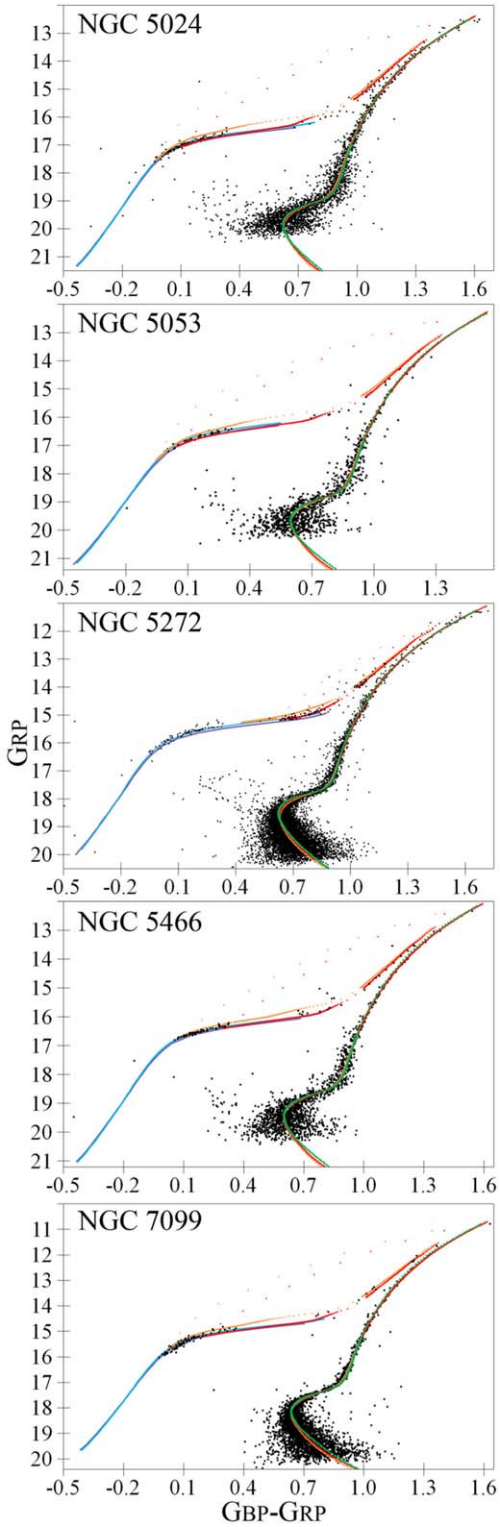

Figure 1. $G_{BP} - G_{RP}$ vs. G_{RP} CMDs for the Gaia DR3 clusters members. The isochrones for $Y = 0.25$ from BaSTI (red), BaSTI ZAHB (purple), and DSED (green), as well as for $Y = 0.275$ from BaSTI (orange) and BaSTI ZAHB (blue), are calculated with the best-fitting parameters from Table 6. RR Lyrae variables are eliminated.

[16] http://classic.sdss.org/dr6/products/value_added/anjohnson08_clusterphotometry.htm. We correct the SDSS magnitudes following An et al. (2009) and Eisenstein et al. (2006).
[17] https://skymapper.anu.edu.au
[18] http://groups.dfa.unipd.it/ESPG/hstphot.html
[19] https://cdsarc.cds.unistra.fr/viz-bin/cat/II/363
[20] https://cdsarc.cds.unistra.fr/viz-bin/cat/J/AJ/116/1775
[21] https://cdsarc.cds.unistra.fr/viz-bin/cat/J/AJ/109/269; *B* photometry is not deep enough.
[22] https://cdsarc.cds.unistra.fr/viz-bin/cat/J/MNRAS/458/4162
[23] https://cdsarc.cds.unistra.fr/viz-bin/cat/J/A+A/290/69

photographic plates taken in the early 1950s at Mt. Palomar and Mt. Wilson Observatories,

14 *BV* photometry of 2294 stars in NGC 5272 with the 2.4 m telescope at Michigan-Dartmouth-MIT (MDM) Observatory (Rey et al. 2001),[24]

15 *BV* photometry of 13955 stars from the original data set of Beccari et al. (2013)[25] or its 1907 Gaia-induced members of NGC 5466 acquired through the blue channel of the Large Binocular Camera (LBC-blue) mounted on the Large Binocular Telescope (LBT), Mount Graham, Arizona,

16 *BVI* photometry of 4708 stars of the original data set of Fekadu et al. (2007) or its 2020 Gaia-induced members of NGC 5466 obtained with the 0.9 m telescope at KPNO,

17 *BV* photometry of 10 633 stars from the original data set of Jeon et al. (2004) or its 1783 Gaia-induced members of NGC 5466 obtained with the 1.8 m telescope at the Bohyunsan Optical Astronomy Observatory in Korea,

18 *VI* photometry of 22 877 stars from the original data set of Sandquist et al. (1999),[26] or its 3135 Gaia-induced members of NGC 7099 obtained with the 4 m telescope at Cerro Tololo Inter-American Observatory (CTIO),

19 J_{2MASS} photometry of 945 Gaia-induced members of NGC 7099 obtained by Cohen et al. (2015) with Infrared Side Port Imager (ISPI) mounted on the 4 m Blanco Telescope at CTIO and calibrated by use of the Two Micron All-Sky Survey (2MASS, Skrutskie et al. 2006) stars,

20 J_{VISTA} photometry with the VISTA Hemisphere Survey with the VIRCAM instrument on the Visible and Infrared Survey Telescope for Astronomy (VISTA, VHS DR5) (McMahon et al. 2013)[27] for 3300 Gaia-induced members of NGC 7099,

21 J_{UKIDSS} photometry with the United Kingdom Infrared Telescope Infrared Deep Sky Survey (UKIDSS) (Hewett et al. 2006)[28] for 6993 Gaia-induced members of NGC 5272.

For some clusters, we use more Gaia-induced members for the SPZ19, PS1, SDSS, VISTA, and UKIDSS CMDs than Gaia cluster members for the Gaia CMDs, since cluster members with less precise Gaia photometry are used in the former but not in the latter case.

[24] https://cdsarc.cds.unistra.fr/viz-bin/cat/J/AJ/122/3219
[25] https://www.lbto.org
[26] https://cdsarc.cds.unistra.fr/viz-bin/cat/J/ApJ/518/262
[27] https://cdsarc.cds.unistra.fr/viz-bin/ReadMe/II/367?format=html&tex=true
[28] http://www.ukidss.org; DSED and BaSTI do not provide isochrones for the J_{VISTA} and J_{UKIDSS} filters, respectively, hence, we substitute these similar filters by each other. We do not use other VISTA and UKIDSS filters, since they cannot be substituted.

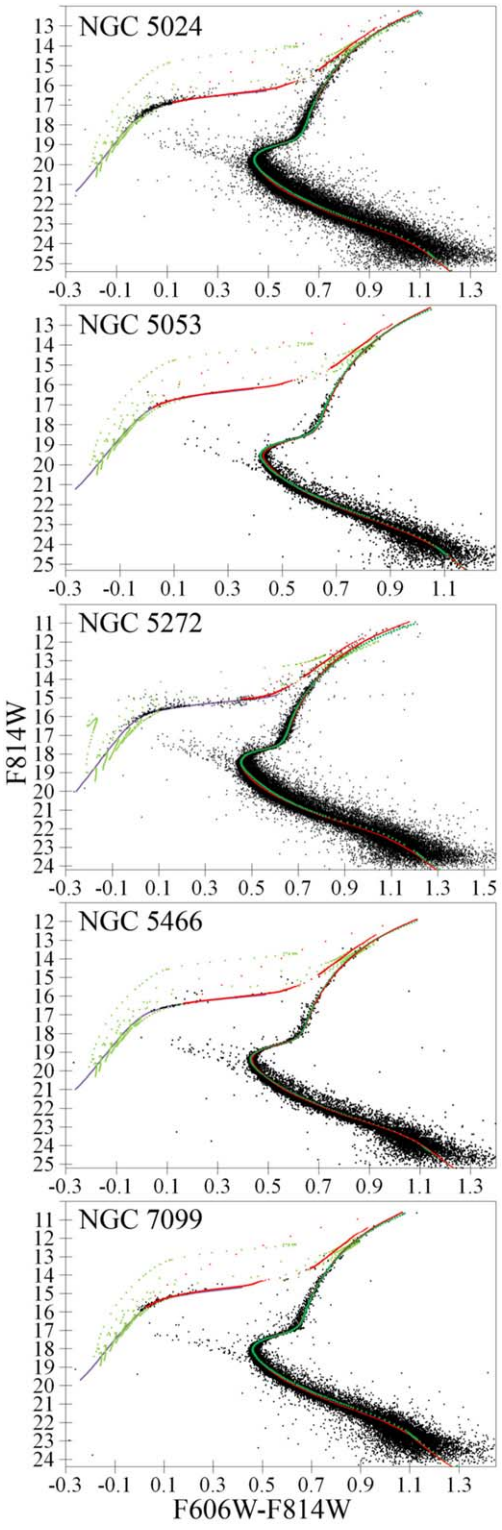

Figure 2. HST/ACS F606W–F814W vs. F814W CMDs for the NLP18 data sets. The isochrones for $Y = 0.25$ from BaSTI (red), BaSTI ZAHB (purple), DSED (green), and DSED HB/AGB (light green) are calculated with the best-fitting parameters from Table 6. RR Lyrae variables are retained.

All the data sets with the same filters are independent, e.g., GCL99 and Massari et al. (2016). The SPZ19 data sets contain photometry from various initial data sets, but not from the others under consideration.

Note that some data sources used in our previous studies provide not enough reliable data for the clusters under consideration: e.g., Parallel-Field Catalogs of the HST UV Legacy Survey of Galactic Globular Clusters (Simioni et al. 2018).

In total, 25, 25, 33, 25, and 27 filters are used for NGC 5024, NGC 5053, NGC 5272, NGC 5466, and NGC 7099, respectively. Each star has photometry in some but not all filters. Table 3 presents the effective wavelength $\lambda_{\rm eff}$ in nm for the used filters, their correspondence with data sets, and the photometric uncertainty cut level. We set the cut level as 3σ of the average photometric uncertainty σ as stated by the authors of the data set, considering that the distribution of photometric uncertainty across each data set is nearly Gaussian. As an exception, we increase the cut level to 0.15 mag for the WISE W1 filter to ensure adequate representation of the TO and bright MS stars. The median uncertainty in photometry across all filters, derived from the data set authors' uncertainty statements, is a few hundredths of a magnitude. Generally, UV and IR photometry is less precise than optical photometry. The uncertainty statements are utilized to assess the statistical uncertainty of our results, though it is demonstrated in Section 3 that the systematic uncertainty is higher.

For cleaning of the data sets, we generally follow the recommendations of their authors to select single star-like objects with reliable photometry. To clean the HST WFC3 and ACS data sets, we select stars with $|\texttt{sharp}| < 0.15$, membership probability >0.9 or -1, and quality fit >0.9. For the SPZ19, GCL99, SDSS, and other data sets with the stated χ and sharp parameters, we select stars with $\chi < 3$ and $|\texttt{sharp}| < 0.3$. For the SMSS DR3 data set, we select star-like objects (i.e., with ClassStar >0.5) and with flags <8. In the Gaia data sets we leave only stars with duplicated_source = 0 (Dup = 0), i.e., sources without multiple source identifiers; astrometric_excess_noise < 1 ($\epsilon i < 1$); a renormalized unit weight error not exceeding 1.4 (RUWE < 1.4); and a corrected excess factor phot_bp_rp_excess_factor (i.e., E(BP/RP)Corr) between -0.14 and 0.14 (Riello et al. 2021).

Some systematic errors dominate in the final uncertainties. This is evident from our comparison of cross-identified data sets with the same or similar filters. For example, the SPZ19 and other *BVI* data sets typically show systematic differences up to 0.04 mag in their colors and magnitudes. Such differences are common, expected, and well-known (see Fekadu et al. 2007, SPZ19 and our previous papers). Some of the differences appear as systematic variations of CMD over the cluster field probably due to photometry zero-point variations, point-spread function variations, telescope focus change, distortion, telescope breathing, stellar generation variations, and other

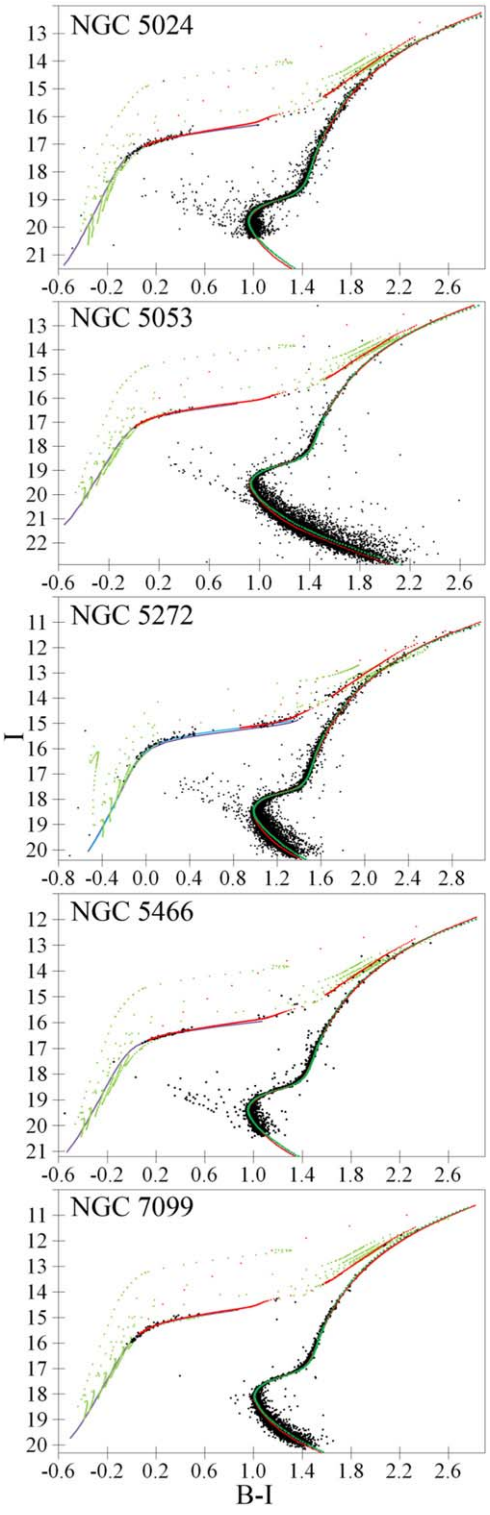

Figure 3. $B - I$ vs. I CMDs for the Gaia cluster members from the SPZ19 data sets (all stars from the SPZ19 data set are for NGC 5053). The isochrones for $Y = 0.25$ from BaSTI (red), BaSTI ZAHB (purple), DSED (green), and DSED HB/AGB (light green), as well as the NGC 5272 BaSTI ZAHB for $Y = 0.275$ (blue) are calculated with the best-fitting parameters from Table 6. RR Lyrae variables are eliminated.

Table 3
The Adopted Effective Wavelength λ_{eff} (nm) for the Filters under Consideration, Numbers of the Data Sets for which the Filters are Used, and Photometric Uncertainty Cut (mag) Applied

Filter	λ_{eff}	Data Sets	Cut
HST/WFC3 F275W	285	1	0.08
HST/WFC3 F336W	340	1	0.07
Strömgren u	349	11, 12	0.08
SDSS u_{SDSS}	360	5	0.20
Landolt U	366	3	0.06
Strömgren v	414	11, 12	0.06
HST/ACS F435W	434	1	0.02
HST/WFC3 F438W	438	1	0.06
HST/WFPC2 F439W	452	7	0.10
Landolt B	452	3, 9, 13–17	0.06
Strömgren b	467	11, 12	0.04
SDSS g_{SDSS}	471	5	0.06
PS1 g_{PS1}	496	4	0.07
Gaia DR3 G_{BP}	505	2	0.10
SMSS g_{SMSS}	514	6	0.06
HST/ACS F555W	541	1	0.02
Strömgren y	548	11, 12	0.04
HST/WFPC2 F555W	551	7	0.10
Landolt V	552	3, 9, 10, 13–18	0.06
HST/ACS F606W	599	1	0.05
Gaia DR3 G	604	2	0.02
SMSS r_{SMSS}	615	6	0.06
SDSS r_{SDSS}	621	5	0.06
PS1 r_{PS1}	621	4	0.06
Landolt R	659	3	0.15
SDSS i_{SDSS}	743	5	0.08
PS1 i_{PS1}	752	4	0.05
Gaia DR3 G_{RP}	770	2	0.10
SMSS i_{SMSS}	776	6	0.06
HST/ACS F814W	807	1	0.05
Landolt I	807	3, 10, 16, 18	0.07
PS1 z_{PS1}	867	4	0.08
SDSS z_{SDSS}	885	5	0.20
SMSS z_{SMSS}	913	6	0.06
PS1 y_{PS1}	971	4	0.14
2MASS J_{2MASS}	1234	19	0.08
UKIDSS J_{UKIDSS}	1250	21	0.12
VISTA J_{VISTA}	1277	20	0.10
*WISE W*1	3317	8	0.15

field systematics, discussed by Anderson et al. (2008). Consequently, these systematics are difficult to separate from DR. Accordingly, the rather high DR in the fields of these clusters (see Table 1) should be considered as a manifestation of the systematics; hence, the higher the DR from a data set, the higher its systematics. Therefore, DR investigation can be used to briefly estimate the systematic quality of the data sets. However, it can be applied only to data sets with sufficient coverage of the cluster fields, i.e., at least 2000 stars. Similar to Paper V, we estimate DR following the method of BCK13. Our DR corrections are generally within ±0.06 mag.

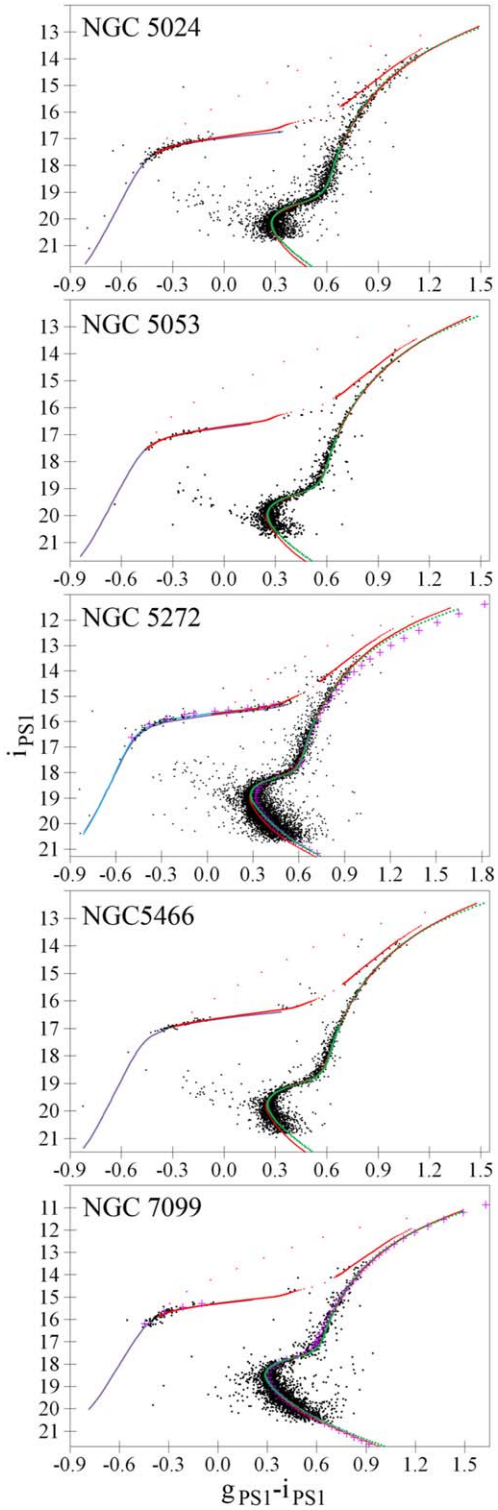

Figure 4. $g_{PS1} - i_{PS1}$ vs. i_{PS1} CMDs for the Gaia cluster members from the PS1 data sets. The fiducial sequences of Bernard et al. (2014) for NGC 5272 and NGC 7099 are displayed as purple crosses. The isochrones for $Y = 0.25$ from BaSTI (red), BaSTI ZAHB (purple), and DSED (green), as well as the NGC 5272 BaSTI ZAHB for $Y = 0.275$ (blue) are calculated with the best-fitting parameters from Table 6. RR Lyrae variables are eliminated.

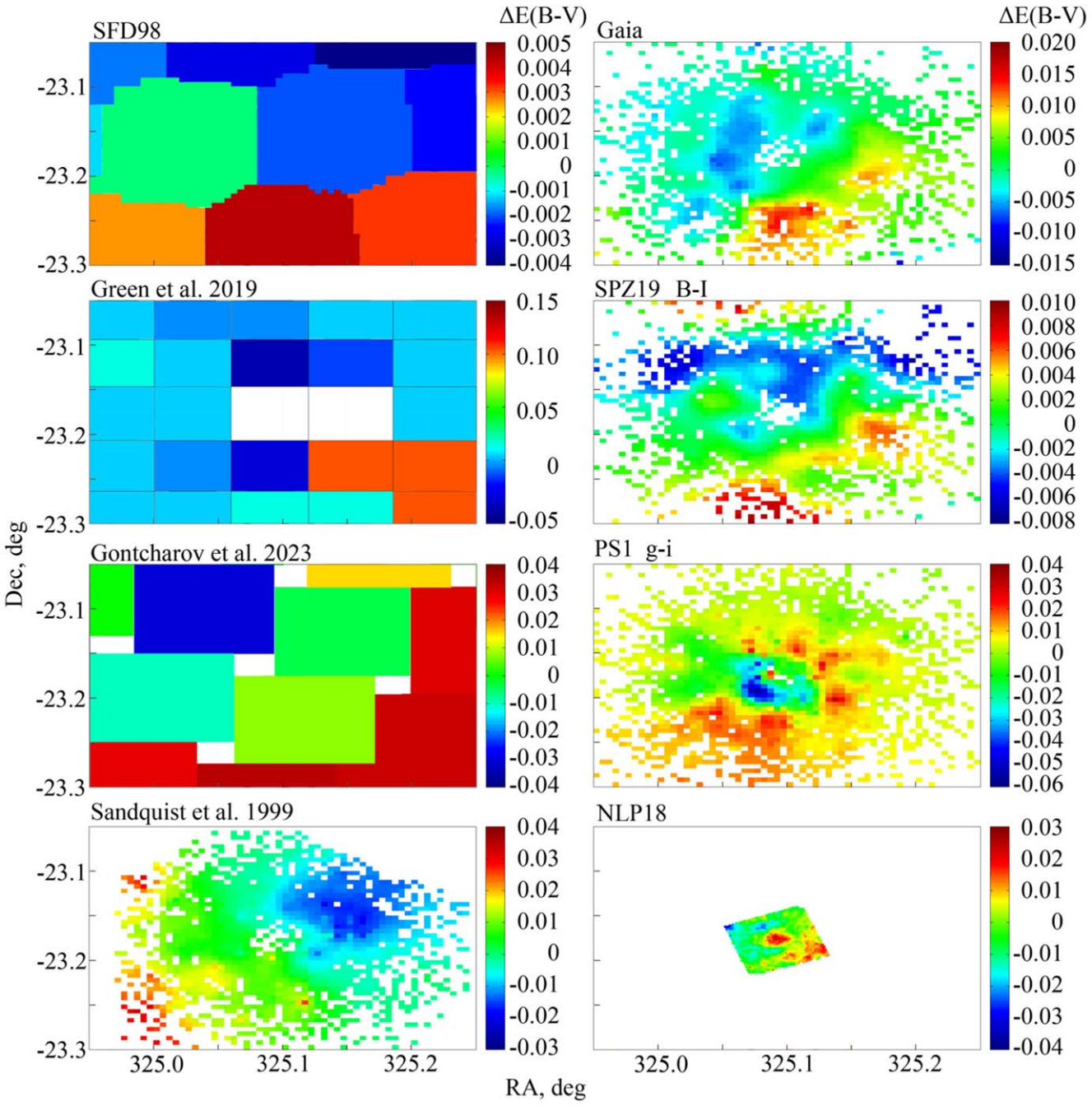

Figure 5. The DR maps, converted into $\Delta E(B-V)$ using the CCM89 extinction law with $R_V = 3.1$, for the same NGC 7099 field from the reddening maps of SFD98, Green et al. (2019), and Gontcharov et al. (2023a) and the data sets of Gaia, SPZ19, PS1, Sandquist et al. (1999), and NLP18. The white areas have no estimates.

It is seen, for example, in Figure 5 with some DR maps for the NGC 7099 field derived from global reddening maps and data sets used. The DR maps do not agree in the DR value (due to systematics in the data) and, hence, we have to show them in Figure 5 on different scales. However, a qualitative similarity is seen for all maps, except that from the Sandquist et al. (1999) data set, which is a reason not to use the latter for our final results. Generally, reddening increases from the upper left (North–West) to the lower right (South-East) corner. This is seen even in the NLP18 map covering only the center of NGC 7099. This can be partially due to an influence of a bright star 41 Cap of $V \approx 5.2$ mag located about 23′ southeast of NGC

7099, i.e., outside the field shown in Figure 5, but not far from its lower right corner. It is worth noting about the map estimates that a very high reddening peak in the lower right corner of the Green et al. (2019) map may be due to some feature of their method in GC fields (Green, private communication), whereas SFD98 probably underestimates the reddening gradient in the cluster field due to a significant gradient of dust temperature in this field.

Among the clusters under consideration, NGC 7099 demonstrates the highest reddening, albeit only slightly higher than the systematics in the data sets. That is why we can see the real NGC 7099 DR manifestation against a background of the systematics. In contrast, the latter completely dominates in the DR maps of the remaining clusters and, hence, these maps have little to do with each other regarding different data sets, and regarding different CMDs/colors of the same data set.

Correction for DR reduces the scatter of stars around their ridge lines or best-fitting isochrones in CMDs. Note that the mean DR correction for each CMD is exactly zero. A smooth and rather low DR for the HST, Gaia, SPZ19, PS1, SDSS, SMSS, GCL99, and Massari et al. (2016) data sets makes them the key data sets for deriving cluster parameters. In contrast, some other data sets demonstrate much more noticeable systematics: e.g., we have to eliminate the brightest stars from the data sets of Buonanno et al. (1994) ($V < 15.2$), Beccari et al. (2013) ($V < 16$), and VISTA ($J_{\rm VISTA} < 12$) due to their unacceptable systematics.

We fit isochrones to a hundred CMDs with different colors. As in our previous papers, the results for adjacent CMDs appear consistent, and they are more reliable for CMDs in the optical range (i.e., with filters within $430 < \lambda_{\rm eff} < 1000$ nm) than for UV, UV–optical, optical–IR, and IR CMDs, such as GCL99 $u-v$, SPZ19 $U-B$, Gaia–VISTA, SPZ19–UKIDSS, PS1–unWISE, UKIDSS–unWISE, and others. Furthermore, uncertainties of the derived reddenings are dominated by the data set systematics, which are irrespective to a wavelength range under consideration in the optical range, while increase in the UV or IR. Therefore, for these low-reddening clusters, the most reliable reddening estimates with the lowest relative uncertainties can be derived from the widest optical wavelength range CMD of each data set. Thus, we derive the final cluster parameters by use of the only key optical CMD for each key data set: (i) F606W–F814W from NLP18, (ii) $G_{\rm BP}-G_{\rm RP}$ from Gaia DR3, (iii) $B-I$ from SPZ19, (iv) $g_{\rm PS1}-i_{\rm PS1}$ from PS1 for all the clusters, and additionally (v) $g_{\rm SDSS}-i_{\rm SDSS}$ from SDSS for all clusters, except NGC 7099, or (v) $g_{\rm SMSS}-i_{\rm SMSS}$ from SMSS for NGC 7099, and also three data sets for NGC 5272: (vi) F435W–F814W from Libralato et al. (2022), (vii) $b-y$ from GCL99, and (viii) $b-y$ from Massari et al. (2016). Thus, we have five key CMDs for all clusters, except NGC 5272, for which we have eight key CMDs.

The remaining data sets and CMDs are also important, since we use their estimates of cluster parameters to evaluate the systematic uncertainty of our results. For example, the key CMDs provide [Fe/H] = −1.95, age 12.15 Gyr, $R = 15.59$ kpc, and $E(B-V) = 0.023$ for NGC 5466, while the addition of the CMDs of Jeon et al. (2004); Fekadu et al. (2007), and Beccari et al. (2013) provides [Fe/H] = −1.92, age 12.03 Gyr, $R = 15.75$ kpc, and $E(B-V) = 0.017$. The differences of these estimates determine the lower limit of their systematic uncertainties: 0.03 dex, 0.12 Gyr, 0.16 kpc, and 0.006 mag, respectively.

As in our previous studies, we also use the cross-identification of data sets to convert the derived reddenings into extinction for each filter we consider, and draw an empirical extinction law (i.e., a dependence of extinction on wavelength) for each combination of cluster, data set, and model. However, for such low-extinction/reddening clusters, empirical extinction law, being based on a ratio of a low extinction to a low reddening, is very uncertain and it is strongly affected by systematic errors of the data sets. These errors appear as deviations of the extinction estimates from an average law in agreement with the systematic color differences in the direct comparison of the data sets. Therefore, we draw the empirical extinction laws using all independent CMDs for the whole wavelength range from the UV to IR in order to verify only whether they agree within the extinction uncertainties with a common (Cardelli et al. 1989, hereafter CCM89) extinction law with $R_{\rm V} = 3.1$.[29]

NGC 5272 and NGC 7099 have optical–IR CMDs covering a wide wavelength range and related to well-defined very low IR extinctions in the VISTA, UKIDSS or unWISE bands. Hence, these CMDs appear especially fruitful for the testing of extinction law. Similar to our previous papers, we calculate extinctions in optical filters from the derived reddenings and IR extinctions. For example,

$$A_{\rm V} = (A_{\rm V} - A_{\rm W1}) + A_{\rm W1} = E(V-{\rm W1}) + A_{\rm W1}, \qquad (1)$$

where $E(V-W1)$ is obtained from a CMD, while very low extinction $A_{\rm W1}$ in the W1 filter is calculated using the CCM89 extinction law with $R_{\rm V} = 3.1$ and optical extinctions and slightly upgraded iteratively with upgrade of the optical extinctions. Finally, the CCM89 extinction law with $R_{\rm V} = 3.1$ appears acceptable for all the clusters, data sets and models. In particular, we use this law to convert the final derived reddenings to the final extinctions $A_{\rm V}$.

[29] Extinction-to-reddening ratio $R_{\rm V} \equiv A_{\rm V}/E(B-V) = 3.1$ is defined for early type MS stars, while the observed ratio $A_{\rm V}/E(B-V)$ depends on intrinsic spectral energy distribution of stars under consideration (Casagrande & VandenBerg 2014). For rather cool and metal-poor stars of the clusters under consideration the observed extinction in the V filter is calculated as $A_{\rm V} = 3.48E(B-V)$, while the extinction coefficients are calculated for the median effective temperature 6400 K of the cluster members.

2.1. Gaia DR3 Cluster Members

Table 1 shows rather different tidal radius estimates for each cluster. Therefore, we consider initial Gaia DR3 samples within initial radii which exceed any previous estimate. We find empirical truncation radii, presented in Table 1, as the radii where the cluster star count surface density drops to the Galactic background. All the data sets are truncated at these radii to reduce contamination from non-members. The truncation allows us to create very clean samples, albeit incomplete. Since all these clusters, except NGC 7099, have tidal tails (Chun et al. 2010; Yang et al. 2023), we might lose several cluster members outside our truncation radii, but it does not affect our results.

As described in our previous studies, accurate Gaia DR3 parallaxes and PMs are used to select cluster members and derive systemic parallaxes and PMs.

As in our previous studies, the final empirical standard deviations of cluster member PMs $\sigma_{\mu_\alpha\cos(\delta)}$ and σ_{μ_δ} are reasonable, but higher by about 20%–70% than the mean stated PM uncertainties, which may mean an underestimation of real errors in the PMs.

Our final weighted mean systemic PMs are presented in Table 4 in comparison to those from Vasiliev & Baumgardt (2021, hereafter VB21) and Vitral (2021) also obtained from Gaia DR3 but by different approaches. Note the different nature of the stated uncertainties: statistical ones for ours and Vitral (2021)'s estimates, while the total (statistical plus systematic) ones for the VB21 estimates. The latter must be adopted as the final, more realistic uncertainties of our PMs. Our PM estimates agree with those from VB21 within ±0.017 mas yr^{-1} and, hence, within the total PM uncertainties. The Vitral (2021)'s estimates for NGC 5024 deviate from the rest significantly, up to 0.095 and 0.062 mas yr^{-1} for the PM components $\mu_\alpha\cos(\delta)$ and μ_δ, respectively.

We correct our median parallaxes of cluster members for the parallax zero-point following Lindegren et al. (2021) and present them in Table 5 for comparison with other estimates in Section 3. We adopt the total uncertainty of Gaia DR3 parallaxes, found by VB21 as 0.01 mas.

Note that NLP18 and Libralato et al. (2022) have cleaned their data sets from non-members by use of dedicated HST PMs. For such high-latitude clusters this cleaning is almost perfect.

2.2. Isochrone-to-data Fitting

Owing to a minor contamination of these high-latitude clusters and the accurate selection of the cluster members, the distribution of stars in our CMDs is well defined. Therefore, as in Paper V, we fit isochrones directly to a bulk of cluster members, without calculation of a fiducial sequence.

We assign a weight to each data point to balance the contributions of different CMD domains. The weight is inversely proportional to the number of stars of a given magnitude, i.e., it reflects the luminosity function of a given data set. For each CMD, modern computers allow us to consider a hundred thousand sets of parameters (Y, [Fe/H], distance, reddening, and age) for a reasonable grid in their five-dimensional space. The grid has steps of 0.025 points, 0.1 dex, 0.05 kpc, 0.001 mag, and 0.5 Gyr for Y, [Fe/H], distance, reddening, and age, respectively. For each set of parameters we calculate the sum of the squares of the residuals between the isochrones and the data points. The best solution, presented in Table 6, is the one with the minimal sum of the squares of the residuals.

As in Paper V, we have to exclude four CMD domains from the direct fitting: the extremely blue HB (i.e., the area bluer than the turn of the observed HB downward), RR Lyrae, other variables, and blue stragglers, marked I, II, III, and IV in Figure 6, respectively. These clusters contain a lot of RR Lyrae and other variables (Arellano Ferro 2022, 2024). Therefore, their detection by Gaia and SPZ19 and subsequent removal are very fruitful for correct determination of the HB magnitude and, hence, cluster distance. Unfortunately, as far as we know, variables are not detected in the HST data sets. Therefore, we approximately determine the areas II and III for the HST data sets and eliminate all stars in them before our fitting,[30] but retain these stars in Figure 2 as an example. The undetected RR Lyrae variables may bias some previous distance estimates.

Figure 6 shows that after the exclusion of these domains, these clusters have enough HB and AGB stars to determine cluster parameters: they are the blue HB stars between the areas I and II, red HB stars between the areas II and III, and AGB

Table 4
The Cluster Systemic PMs (mas yr^{-1})

Cluster	Source	$\mu_\alpha\cos(\delta)$	μ_δ
	This study	-0.150 ± 0.013	-1.336 ± 0.011
NGC 5024	VB21	-0.134 ± 0.024	-1.331 ± 0.024
	Vitral (2021)	-0.229 ± 0.008	-1.274 ± 0.008
	This study	-0.333 ± 0.016	-1.224 ± 0.017
NGC 5053	VB21	-0.329 ± 0.026	-1.214 ± 0.025
	Vitral (2021)	-0.325 ± 0.011	-1.209 ± 0.011
	This study	-0.150 ± 0.005	-2.671 ± 0.004
NGC 5272	VB21	-0.152 ± 0.022	-2.670 ± 0.023
	Vitral (2021)	-0.151 ± 0.004	-2.667 ± 0.004
	This study	-5.360 ± 0.012	-0.828 ± 0.010
NGC 5466	VB21	-5.343 ± 0.024	-0.823 ± 0.024
	Vitral (2021)	-5.368 ± 0.008	-0.838 ± 0.008
	This study	-0.735 ± 0.011	-7.284 ± 0.009
NGC 7099	VB21	-0.738 ± 0.025	-7.299 ± 0.025
	Vitral (2021)	-0.737 ± 0.006	-7.293 ± 0.006

[30] We cannot eliminate the variables, known from the Gaia and SPZ19 data sets, by their cross-identification with the HST data sets, since these data sets cover different parts of the cluster fields and, hence, have little, if any, common variables.

Table 5
Parallax Estimates (mas) with their Total (Statistical and Systematic) Uncertainties for Clusters under Consideration

Parallax	NGC 5024	NGC 5053	NGC 5272	NGC 5466	NGC 7099
VB21, Gaia DR3 astrometry	0.064 ± 0.011	0.047 ± 0.011	0.106 ± 0.010	0.053 ± 0.011	0.132 ± 0.011
BV21, various methods	0.054 ± 0.001	0.057 ± 0.001	0.098 ± 0.001	0.062 ± 0.001	0.118 ± 0.001
This study, Gaia DR3 astrometry	0.066 ± 0.011	0.041 ± 0.015	0.110 ± 0.010	0.062 ± 0.011	0.119 ± 0.011
This study, isochrone fitting	0.055 ± 0.002	0.059 ± 0.002	0.099 ± 0.003	0.064 ± 0.002	0.121 ± 0.004

Table 6
The Results of our Isochrone Fitting for Two Models and Some Key CMDs

	BaSTI				DSED			
Data set and color	[Fe/H]	Age	R	Reddening	[Fe/H]	Age	R	Reddening
				NGC 5024				
NLP18 F606W–F814W	−1.9	12.5	18.3	0.018 [0.018]	−1.9	13.0	18.0	0.027 [0.028]
Gaia $G_{BP} - G_{RP}$	−1.9	13.0	18.0	0.043 [0.031]	−1.9	12.5	18.3	0.071 [0.051]
SPZ19 $B - I$	−1.9	13.0	18.5	0.015 [0.007]	−1.9	13.0	18.3	0.036 [0.017]
PS1 $g_{PS1} - i_{PS1}$	−2.0	13.0	18.2	0.040 [0.025]	−2.0	13.5	18.0	0.032 [0.022]
…	…	…	…	…	…	…	…	…
				NGC 5053				
NLP18 F606W–F814W	−2.2	12.5	17.2	0.018 [0.018]	−2.2	12.5	17.2	0.022 [0.023]
Gaia $G_{BP} - G_{RP}$	−2.1	12.5	17.0	0.038 [0.027]	−2.0	12.5	17.0	0.055 [0.039]
SPZ19 $B - I$	−2.2	12.5	17.2	0.033 [0.017]	−2.1	13.0	16.8	0.032 [0.016]
PS1 $g_{PS1} - i_{PS1}$	−2.1	13.0	17.0	0.020 [0.013]	−2.0	13.5	16.7	0.008 [0.005]
…	…	…	…	…	…	…	…	…
				NGC 5272				
NLP18 F606W–F814W	−1.5	11.5	10.1	0.014 [0.014]	−1.5	11.5	10.0	0.027 [0.028]
Gaia $G_{BP} - G_{RP}$	−1.5	11.5	10.0	0.031 [0.022]	−1.6	11.0	10.2	0.073 [0.052]
SPZ19 $B - I$	−1.6	11.5	10.3	0.023 [0.011]	−1.6	11.5	10.1	0.061 [0.029]
PS1 $g_{PS1} - i_{PS1}$	−1.7	12.0	10.2	0.031 [0.020]	−1.6	12.0	10.1	0.031 [0.020]
…	…	…	…	…	…	…	…	…
				NGC 5466				
NLP18 F606W–F814W	−1.9	12.0	15.6	0.015 [0.015]	−2.0	12.5	15.6	0.024 [0.025]
Gaia $G_{BP} - G_{RP}$	−1.9	11.5	15.6	0.042 [0.030]	−1.9	12.0	15.6	0.069 [0.049]
SPZ19 $B - I$	−2.0	12.5	15.6	0.038 [0.018]	−2.0	12.5	15.5	0.057 [0.027]
PS1 $g_{PS1} - i_{PS1}$	−2.0	12.0	15.7	0.029 [0.019]	−1.9	12.5	15.4	0.022 [0.014]
…	…	…	…	…	…	…	…	…
				NGC 7099				
NLP18 F606W–F814W	−2.2	13.0	8.3	0.040 [0.041]	−2.2	13.5	8.2	0.050 [0.050]
Gaia $G_{BP} - G_{RP}$	−1.9	12.5	8.2	0.062 [0.044]	−1.9	12.0	8.3	0.087 [0.062]
SPZ19 $B - I$	−2.1	13.0	8.4	0.079 [0.037]	−2.2	13.5	8.3	0.100 [0.047]
PS1 $g_{PS1} - i_{PS1}$	−2.1	13.0	8.3	0.066 [0.043]	−2.1	13.0	8.4	0.058 [0.038]
…	…	…	…	…	…	…	…	…

Note. In all the CMDs, the color is the abscissa, the reddening is the color excess, and the magnitude in the redder filter is the ordinate. Each derived reddening is followed by corresponding $E(B-V)$, given in parentheses and calculated using extinction coefficients from Casagrande & VandenBerg (2014, 2018b, 2018a) or CCM89 with $R_V = 3.1$. [Fe/H] is given only for CMDs, which allow its calculation as a fitting parameter. Age is in Gyr, R is in kpc. The complete table is available online.

stars on the red side of area III. As noted earlier, the blue HB stars of NGC 5272 are better fitted with $Y = 0.275$. Another domain better fitted with $Y = 0.275$ is the faint RGB, marked V in Figure 6.

We present some key CMDs with isochrone fits in Figures 1–4. Other CMDs are presented online or can be provided on request.

3. Results

Table 7 presents our estimates of [Fe/H], age, distance, distance modulus $(m-M)_0$, apparent V-band distance modulus $(m-M)_V$, and $E(B-V)$ averaged for the key CMDs. We provide the uncertainties after the values as standard deviations of one estimate in order to emphasize a good agreement

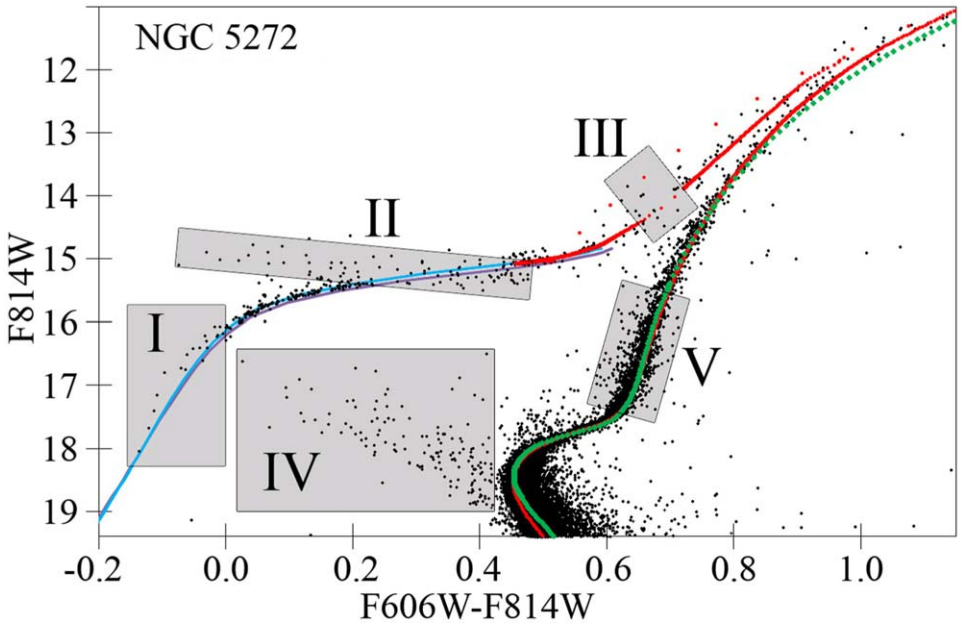

Figure 6. A central part of the F606W–F814W vs. F814W CMD from the NLP18 data set for NGC 5272. The isochrones from BaSTI (red) and DSED (green) for $Y = 0.25$, the BaSTI ZAHB for $Y = 0.25$ (purple) and for $Y = 0.275$ (blue) are calculated with the best-fitting parameters from Table 6. The gray areas are the CMD domains of the (I) extremely blue HB, (II) RR Lyrae, (III) other variables, (IV) blue stragglers, and (V) faint RGB, which are discussed in the text.

between the models seen in the fact that the standard deviation of the combined BaSTI plus DSED sample is comparable with the model standard deviations. The standard deviation of the average value (i.e., the standard deviation of one estimate divided by the square root of the number of estimates), half the difference between the model estimates, and systematic uncertainty of the average value are given in separate columns.

As in Paper V, we assign the systematic uncertainty to our [Fe/H] and age estimates as 0.1 dex and 0.8 Gyr, respectively. The systematic uncertainties of distance and apparent V-band distance modulus are calculated from that of distance modulus, which is assigned as 0.07 mag. This is a conservative estimate of all possible systematic effects on the magnitude of the HB and AGB stars, which is the basis for distance estimates.

The systematic uncertainty of [Fe/H] is the dominant contributor to the systematic uncertainties of our reddening and extinction estimates, resulting in values equivalent to $\sigma_{E(B-V)} = 0.01$ and $\sigma_{A_V} = 0.03$ mag, respectively. The former is presented in Table 7 as "Systematics." The systematic uncertainties of our reddening estimates, arising from imperfections in the models, can be assessed by calculating half the difference between the models presented in Table 7 as "Model Δ." It is seen that this model systematic term is less significant than that of [Fe/H], with the exception of NGC 5272. It is worth noting that the absence of highly negative derived reddenings (see Table 6) confirms the reliability of the isochrones, at least, for the optical filters.

Our [Fe/H] estimates support lower [Fe/H] estimates from the literature for NGC 5272 [such as the one of Arellano Ferro (2024) from Table 1, based on their RR Lyrae calibration, and all from Table 2, except the one of Stenning et al. (2016)], while higher [Fe/H] estimates for the remaining low-metallicity clusters [such as those of Mészáros et al. (2020), photometric ones of Jurcsik & Hajdu (2023), and the ones of Arellano Ferro (2024), based on their RR Lyrae calibration, from Table 1, as well as some from Table 2]. Accordingly, our estimates support the arguments of Mucciarelli & Bonifacio (2020) in favor of photometrically and against spectroscopically derived [Fe/H] of low-metallicity GCs.

Also, we conclude that three clusters (NGC 5024, NGC 5053, and NGC 7099) have nearly the same old age, NGC 5466 is younger, while NGC 5272 is much younger. This qualitatively agrees with only Dotter et al. (2010) among the estimates in Table 1, albeit NGC 5272 always tends to be rather young. Age estimates from Table 1 are good representatives of recent age estimates from the literature, which are not consistent even in relative age estimates: for example, NGC 5272 is older than NGC 5466 by Valcin et al. (2020), while slightly younger by Dotter et al. (2010) and much younger by Forbes & Bridges (2010); NGC 7099 is older than NGC 5024 and NGC 5053 by VandenBerg et al. (2013), while it is younger by Valcin et al. (2020). Anyway, our age estimates agree with all the estimates within their uncertainties.

Since distance estimates from the literature (e.g., in a comprehensive compilation of BV21) are rather diverse for

Table 7
Our [Fe/H] (dex), Age (Gyr), Distance (kpc), Distance Modulus (mag), Apparent V-band Distance Modulus (mag), and $E(B-V)$ (mag) Estimates Averaged from the Key CMDs

Cluster	BaSTI	DSED	Average Value	σ	Model Δ	Systematic
			[Fe/H]			
NGC 5024	-1.92 ± 0.04	-1.94 ± 0.05	-1.93 ± 0.05	0.02	0.01	0.10
NGC 5053	-2.12 ± 0.08	-2.04 ± 0.11	-2.08 ± 0.10	0.03	0.04	0.10
NGC 5272	-1.58 ± 0.07	-1.63 ± 0.09	-1.60 ± 0.08	0.02	0.03	0.10
NGC 5466	-1.96 ± 0.05	-1.94 ± 0.05	-1.95 ± 0.05	0.02	0.01	0.10
NGC 7099	-2.04 ± 0.13	-2.10 ± 0.12	-2.07 ± 0.13	0.04	0.03	0.10
			Age			
NGC 5024	12.90 ± 0.22	13.10 ± 0.42	13.00 ± 0.33	0.11	0.10	0.80
NGC 5053	12.60 ± 0.22	12.80 ± 0.45	12.70 ± 0.35	0.11	0.10	0.80
NGC 5272	11.69 ± 0.26	11.56 ± 0.32	11.63 ± 0.29	0.07	0.06	0.80
NGC 5466	12.00 ± 0.35	12.30 ± 0.27	12.15 ± 0.34	0.11	0.15	0.80
NGC 7099	12.70 ± 0.45	12.90 ± 0.65	12.80 ± 0.54	0.17	0.10	0.80
			Distance			
NGC 5024	18.28 ± 0.19	18.16 ± 0.15	18.22 ± 0.18	0.06	0.06	0.60
NGC 5053	17.08 ± 0.11	16.90 ± 0.20	16.99 ± 0.18	0.06	0.09	0.56
NGC 5272	10.11 ± 0.16	10.05 ± 0.16	10.08 ± 0.16	0.04	0.03	0.33
NGC 5466	15.64 ± 0.05	15.54 ± 0.09	15.59 ± 0.09	0.03	0.05	0.51
NGC 7099	8.26 ± 0.11	8.32 ± 0.08	8.29 ± 0.10	0.03	0.03	0.27
			Distance modulus			
NGC 5024	16.31 ± 0.02	16.30 ± 0.02	16.30 ± 0.02	0.01	0.01	0.07
NGC 5053	16.16 ± 0.01	16.14 ± 0.03	16.15 ± 0.02	0.01	0.01	0.07
NGC 5272	15.02 ± 0.03	15.01 ± 0.04	15.02 ± 0.03	0.01	0.01	0.07
NGC 5466	15.97 ± 0.01	15.96 ± 0.01	15.96 ± 0.01	0.01	0.01	0.07
NGC 7099	14.58 ± 0.03	14.60 ± 0.02	14.59 ± 0.03	0.01	0.01	0.07
			Apparent V-band distance modulus			
NGC 5024	16.37 ± 0.02	16.39 ± 0.05	16.38 ± 0.04	0.01	0.01	0.08
NGC 5053	16.21 ± 0.04	16.20 ± 0.07	16.21 ± 0.05	0.02	0.01	0.08
NGC 5272	15.07 ± 0.03	15.13 ± 0.06	15.10 ± 0.05	0.01	0.03	0.08
NGC 5466	16.04 ± 0.02	16.05 ± 0.05	16.05 ± 0.04	0.01	0.01	0.08
NGC 7099	14.73 ± 0.03	14.77 ± 0.03	14.75 ± 0.03	0.01	0.02	0.08
			$E(B-V)$			
NGC 5024	0.018 ± 0.011	0.028 ± 0.013	0.023 ± 0.013	0.004	0.005	0.010
NGC 5053	0.015 ± 0.010	0.018 ± 0.014	0.017 ± 0.011	0.004	0.002	0.010
NGC 5272	0.013 ± 0.007	0.033 ± 0.016	0.023 ± 0.016	0.004	0.010	0.010
NGC 5466	0.019 ± 0.006	0.027 ± 0.013	0.023 ± 0.011	0.003	0.004	0.010
NGC 7099	0.041 ± 0.003	0.048 ± 0.009	0.045 ± 0.007	0.002	0.003	0.010

Note. The $E(B-V)$ estimates are calculated from the derived reddenings by use of extinction coefficients from Casagrande & VandenBerg (2014, 2018b, 2018a) or CCM89 with $R_V = 3.1$. The uncertainties after the values are standard deviations of one estimate. "σ," "Model Δ" and "Systematics" are the standard deviation of the average value, half the difference between the models, and systematic uncertainty of the average value, respectively.

these clusters, our distance estimates agree with some of them, but disagree with some others. Examples of former and latter, presented in Table 1, are the estimates of Arellano Ferro (2024), obtained from their calibrations for the RRc stars,[31] and Hunt & Reffert (2023) obtained by a sophisticated method. However, the most important is that our distance estimates agree with the most probable compiled distance estimates of BV21 presented in Table 1 within 1.0σ, 1.8σ, 0.9σ, 2.5σ, and 1.5σ of their stated statistical uncertainties for NGC 5024, NGC 5053, NGC 5272, NGC 5466, and NGC 7099, respectively, and well inside the systematic uncertainties for all the clusters, except NGC 5466. This may mean that each method of distance determination could have significant systematics for such distant and RR Lyrae-contaminated clusters, while a compilation of estimates from different methods can provide a much more accurate result.

The same conclusion is derived from comparing parallaxes obtained through various methods. We convert the distances and their total uncertainties from our isochrone-fitting into parallaxes and their corresponding uncertainties. These are then compared in Table 5 with parallaxes obtained from our analysis and VB21, both derived from Gaia DR3 astrometry. Additionally, we compare them with parallaxes converted from the BV21 compiled distances, which were obtained using

[31] A good agreement of our estimates with those of Arellano Ferro (2024) for both R and [Fe/H] suggests that his calibrations for RRc variables are robust, whereas his recommendation to calibrate RRab and RRc variables separately is valid.

Table 8
The Relative Estimates Presented as Cluster Sequences along Ascending or Descending Parameters

Parameter	Sequence
Δ[Fe/H] (dex) from metal-poor to metal-rich	NGC 5053 - **0.02** - NGC 7099 - **0.14** - NGC 5466 - **0.02** - NGC 5024 - **0.35** - NGC 5272
ΔAge (Gyr) from old to young	NGC 5024 - **0.00** - NGC 7099 - **0.19** - NGC 5053 - **0.56** - NGC 5466 - **0.63** - NGC 5272
ΔR (kpc) from distant to nearby	NGC 5024 - **1.19** - NGC 5053 - **1.43** - NGC 5466 - **5.45** - NGC 5272 - **1.83** - NGC 7099
Δ$E(B-V)$ (mag) from less to more reddened	NGC 5053 - **0.005** - NGC 5024 - **0.000** - NGC 5272 - **0.000** - NGC 5466 - **0.020** - NGC 7099

various methods and presented in Table 1. A moderate agreement between the parallaxes is seen.

The total uncertainty of any astrometric estimate of Gaia DR3 parallax cannot be better than 0.01 mas (Vasiliev & Baumgardt 2021), while the total uncertainty of isochrone-fitting parallax decreases with R (so that the relative parallax uncertainty is constant). Therefore, Table 5 shows that the parallax estimates from the Gaia DR3 astrometry are less precise than those from our isochrone fitting for such distant clusters.

Comparing our reddening estimates with those in Tables 1 and 2, we conclude that our estimates are higher than those of Harris (1996) and Schlafly & Finkbeiner (2011) for some of the clusters, higher than all estimates of Lallement et al. (2019), agree with the estimates of Schlegel et al. (1998, hereafter SFD98), Meisner & Finkbeiner (2015), and Dotter et al. (2010), while generally lower than the estimates of Green et al. (2019); Gontcharov et al. (2023a), and Paust et al. (2010).

Our final extinction A_V estimates are 0.08 ± 0.01, 0.06 ± 0.01, 0.08 ± 0.01, 0.08 ± 0.01, and 0.16 ± 0.01 mag (with the systematic uncertainty 0.03 mag) for NGC 5024, NGC 5053, NGC 5272, NGC 5466, and NGC 7099, respectively.

Four of our five clusters are very close to the North Galactic Pole. Three of them show $A_V = 0.08$ mag. Hence, this value can be accepted as a reliable estimate of the total Galactic extinction across the whole dust layer above the Sun. Note that the total Galactic extinction below the Sun (i.e., at the South Galactic Pole) should be a few hundredths of a magnitude higher, since the midplane of the Galactic dust layer is below the Sun.

Similar to our previous papers, we consider the relative estimates for the cluster parameters separately derived for each model. Systematic errors of the models must be canceled out in such relative estimates. We use four key CMDs available for all the clusters: (i) F606W–F814W from NLP18, (ii) $G_{BP} - G_{RP}$ from Gaia DR3, (iii) $B - I$ from SPZ19, and (iv) $g_{PS1} - i_{PS1}$ from PS1. Table 8 presents the relative estimates of the derived parameters as cluster sequences. Adopting 0.1 dex, 0.4 Gyr, 0.2 kpc, and 0.01 mag as the uncertainties of the relative estimates of [Fe/H], age, distance and reddening, respectively, we conclude from Table 8 that (i) NGC 5272 is more metal-rich than the remaining clusters of nearly the same [Fe/H] ≈ -2; (ii) three clusters have nearly the same old age, while NGC 5466 is younger and NGC 5272 is much younger; (iii) NGC 7099 has a higher reddening than the remaining clusters with nearly the same very low reddening. Thus, the most important conclusion is that NGC 5024, NGC 5053, and NGC 7099 have nearly the same metallicity and age. Moreover, these clusters have similar low helium enrichments. Hence, their HB morphology difference should be explained by other parameters besides metallicity, age, or helium enrichment.

Table 9
The Count of the Blue HB, RR Lyrae and Red HB Stars and HB Type of the Clusters

Cluster	Data Set	Blue HB	RR Lyrae	Red HB	HB Type
NGC 5024	Gaia	188	34	3	0.82 ± 0.14
NGC 5024	SPZ19	263	39	6	0.83 ± 0.12
NGC 5053	Gaia	34	8	1	0.77 ± 0.18
NGC 5053	SPZ19	35	9	2	0.72 ± 0.17
NGC 5272	Gaia	79	91	61	0.08 ± 0.13
NGC 5272	SPZ19	89	97	61	0.11 ± 0.13
NGC 5466	Gaia	65	19	8	0.62 ± 0.08
NGC 5466	SPZ19	65	18	8	0.63 ± 0.08
NGC 7099	Gaia	82	5	4	0.86 ± 0.14
NGC 7099	SPZ19	74	5	6	0.80 ± 0.15

3.1. HB Morphology

We calculate the HB types of the clusters by use of the Gaia and SPZ19 data sets, which allow us a robust determination of RR Lyrae variables by the `VarFlag` parameter in the former and `Vary` (Welch-Stetson variability index) and `Weight` (weight of the variability index) parameters in the latter data sets. Table 9 shows the count of the blue HB stars, RR Lyrae variables and red HB stars, used in our HB type calculation. The derived HB types are similar for different data sets of the same cluster. The HB type uncertainties are calculated by our Monte-Carlo simulation. The mean values of the HB types are presented in Table 1, where they can be compared with the HB type estimates from Torelli et al. (2019) and Arellano Ferro (2024). A good agreement is seen for NGC 5024, NGC 5466, and NGC 7099.

Our HB type estimates for NGC 5024, NGC 5272, and NGC 7099 may be underestimated due to a strong incompleteness of the Gaia and SPZ19 data sets in crowded centers of these clusters, where many blue HB stars exist (Catelan 2009). Our

Table 10
Some Parameters of the Distribution of the HB Stars on Mass and Preceding Mass Loss

Cluster	$M_{Y=0.25}$	$M_{Y=0.275}$	$M_{\rm Gratton2010}$	μ_{1G}	μ_{2G}	η	$N_{\rm least}$
NGC 5024	0.670 ± 0.005	0.640 ± 0.005	0.638 ± 0.002	0.100 ± 0.017	0.120 ± 0.019	0.26 ± 0.02	$\leqslant 15$
NGC 5053	0.700 ± 0.005	0.660 ± 0.005	0.674 ± 0.001	0.116 ± 0.014	⋯	0.32 ± 0.02	$\leqslant 1$
NGC 5272	0.680 ± 0.005	0.670 ± 0.005	0.624 ± 0.003	0.188 ± 0.017	0.240 ± 0.022	0.46 ± 0.02	$\leqslant 15$
NGC 5466	0.700 ± 0.005	0.670 ± 0.005	0.687 ± 0.020	0.103 ± 0.017	0.119 ± 0.023	0.26 ± 0.02	$\leqslant 1$
NGC 7099	0.680 ± 0.005	0.650 ± 0.005	0.644 ± 0.004	0.066 ± 0.014	0.083 ± 0.019	0.19 ± 0.02	$\leqslant 4$

Note. $M_{Y=0.25}$ and $M_{Y=0.275}$ are the minimum HB masses within regular stellar evolution for $Y = 0.25$ and 0.275, respectively, $M_{\rm Gratton2010}$ is the empirical minimum HB mass estimate from Gratton et al. (2010), μ_{1G} and μ_{2G} are the mass loss for the first and second generation stars, respectively, from Tailo et al. (2020), η is the parameter in Reimers' law of mass loss (Reimers 1975) taken from Tailo et al. (2020), and $N_{\rm least}$ is the number of observed HB stars with mass lower than $M_{\rm Gratton2010}$. All masses are in solar mass.

underestimation of the blue HB star counts in these clusters is evident from a comparison of their counts in Table 2 of Torelli et al. (2019) and Table 9. The comparison of these tables also shows that no such underestimation occurs for loose clusters NGC 5053 and NGC 5466, whose fields are well covered by the Gaia and SPZ19 data sets. However, even a strong underestimation of the blue HB star count by a hundred stars would bias the HB type by only a few hundredths, i.e., imperceptibly.

A bias of the HB type estimates of Torelli et al. (2019) due to imperfect identification of cluster members and RR Lyrae variables seems to be more significant. Indeed, Torelli et al. (2019) count zero, eight, and five red HB stars in NGC 5024, NGC 5053, and NGC 5466, respectively, in contrast to our counts of six, two, and eight presented in Table 9. One can compute that the difference between these counts significantly affects the HB type estimates. Therefore, we check properties of all stars, star-by-star, in this sparsely populated red HB domain of these clusters taking into account also red HB stars from the NLP18 data sets covering the central parts of these clusters. As a result, we conclude that our counts of the red HB stars in NGC 5024, NGC 5053, and NGC 5466 are more reliable, while those of Torelli et al. (2019) seem to be wrong. In particular, NGC 5466 has more red HB stars than NGC 5053 (this may indicate that the former is younger than the latter), while most of the eight Torelli et al. (2019)'s red HB stars in NGC 5053 are variables or non-members. This is the reason for a significant difference between our and Torelli et al. (2019) HB types for NGC 5053, while such a difference for NGC 5272 is explained by the loss of much more blue than red HB stars in the crowded center of NGC 5272 due to the above mentioned strong incompleteness of the Gaia and SPZ19 data sets there. We conclude that the HB type of NGC 5053 must be rather close to those of NGC 5024 and NGC 7099.[32] This perfectly agrees with our earlier conclusion that these three clusters have nearly the same [Fe/H], age and helium abundance. Moreover, our estimate of slightly younger age of NGC 5466 and much younger age of NGC 5272 agrees with their lower HB types. Thus, at first glance, the HB morphology difference of these clusters does not contradict the suggestion that [Fe/H] and age are the first and second HB parameters respectively.

Table 10 describes some parameters of the HB star distribution on mass and preceding mass loss.

Regular stellar evolution without an extreme mass loss produces the HB and AGB stars within a certain range of mass, effective temperature, and color, which uniquely correspond to each other: mass increases with decreasing temperature and increasing color from the left to right side of the CMDs in Figures 1–4. The range of mass is predicted, for example, by the best-fitting BaSTI isochrones describing regular stellar evolution for $Y = 0.25$ and 0.275, i.e., the red and orange curves, respectively, in Figures 1–4. The maximum HB mass within regular stellar evolution, about 0.8 solar mass, is nearly the same for these low-metallicity and old clusters.[33] The minimum HB masses within regular stellar evolution $M_{Y=0.25}$ and $M_{Y=0.275}$ for $Y = 0.25$ and 0.275, respectively, are based on the best-fitting BaSTI isochrones, averaged for all the key data sets and presented in Table 10. Note that $M_{Y=0.25} > M_{Y=0.275}$. The observed distribution of the HB stars between the maximum and minimum masses corresponds to a theoretical distribution from BaSTI. In particular, Figures 1–4 show that the oldest and low-metallicity NGC 5024, NGC 5053, and NGC 7099 have much more stars at the blue side (i.e., between the areas I and II in terms of Figure 6) of the red and orange BaSTI isochrones in the HB domain than at their red side (i.e., between the areas II and III in terms of Figure 6), while younger NGC 5466 and NGC 5272 have comparable numbers of stars at the sides. Thus, for each cluster, $M_{Y=0.25}$ and $M_{Y=0.275}$ are the unambiguous characteristics of the HB stars within regular stellar evolution.

There may be HB stars with a mass lower than $M_{Y=0.275}$. They are seen in Figures 1–4 along the BaSTI ZAHB purple and blue

[32] $\Delta(V-I)$, $\tau_{\rm HB}$ and HB type from Table 1 correlate for these clusters. After our analysis of the NGC 5053 HB type bias, we propose that the $\Delta(V-I)$ and $\tau_{\rm HB}$ HB morphology indexes of this loose cluster may also be biased and should be revised.

[33] To compare the clusters, we show the BaSTI ZAHBs in Figures 1–4 for nearly the same range of 0.5–0.8 solar mass from the left to right side of the ZAHB curve.

curves to the left (i.e., bluer) of the regular BaSTI isochrone red and orange curves. NGC 5272 has many such stars,[34] while the remaining clusters have only a few. Accordingly, the empirical minimum HB mass estimates $M_{\rm Gratton2010}$ from Gratton et al. (2010), defined as the values including 90% of the observed distribution of the HB stars and presented in Table 10, are close to $M_{Y=0.275}$ for all the clusters, except NGC 5272 with $M_{Y=0.275} \gg M_{\rm Gratton2010}$.[35] Hence, the HB morphology of NGC 5272 must be explained either by a very high helium enrichment, which is not observed for this cluster, or an extreme mass loss between the MS and HB, while the HB morphology of the remaining clusters does not need such an additional parameter. This agrees with the estimates by Tailo et al. (2020) of mass loss for the first (μ_{1G}) and second (μ_{2G}) generation of stars and corresponding parameter η in Reimers' law (Reimers 1975) for the first generation stars presented in Table 10 for all the clusters. It is seen that the mass-loss efficiency in NGC 5272 is much higher than in the remaining clusters. Note that the blue HB stars with a higher $Y \approx 0.275$ belong to the second generation of NGC 5272 with very high mass loss.[36]

The observed distribution of the HB stars on mass often resembles a Gaussian distribution (Catelan 2009) in accordance with the stochastic mass loss between the MS and HB considered by BaSTI. This suggests a smooth decrease of the HB star count with the decrease of their mass. Otherwise, an additional parameter is needed in order to explain an abrupt distribution at the minimum HB mass for some clusters. Such an abrupt distribution can be seen as the absence or very low number of low-mass HB stars to the left of the best-fitting BaSTI isochrone of regular stellar evolution, i.e., when $M_{\rm Gratton2010}$ is rather high and $M_{Y=0.275} < M_{\rm Gratton2010}$. Table 10 shows this for NGC 5053 and NGC 5466. Also, such an abrupt distribution can be seen as a very small number $N_{\rm least}$ (presented in Table 10) of observed HB stars with mass lower than $M_{\rm Gratton2010}$ (most of these stars are at the centers of the clusters and observed only by the HST). Thus, Table 10 shows that NGC 5053, NGC 5466, and NGC 7099 have a rather abrupt distribution at the minimum HB mass.[37] This may be due to the action of one more parameter after metallicity, age, and mass-loss efficiency. Namely, NGC 5053, NGC 5466, and NGC 7099 have lost their low-mass stars, including the bluest HB stars, due to dynamical evolution and mass segregation. It seems that both core-collapse and loose clusters lose low-mass stars more effectively than clusters with a medium star concentration. The low-mass stars are eliminated from the loose clusters NGC 5053 and NGC 5466 by Galactic potential, while from NGC 7099 by its core collapse (Meylan & Heggie 1997; Odenkirchen & Grebel 2004; Lauchner et al. 2006; Fekadu et al. 2007; Beccari et al. 2015; Kimmig et al. 2015; Sollima et al. 2017; Mansfield et al. 2022). In particular, the large tidal tails of NGC 5053 and NGC 5466 suggest that these clusters have been strongly disrupted by interactions with the Galaxy or its satellites. Thus, it seems that the HB morphology difference of the clusters under consideration can be completely explained by four parameters: metallicity, age, mass-loss efficiency, and loss of low-mass stars in cluster evolution.

Note that the pair NGC 7099 and NGC 5024 is very similar in its HB morphology difference to the pair NGC 6397 and NGC 6809 from Paper V as pairs of core-collapse and non-core-collapse clusters of similar metallicity, age, helium abundance, and mass-loss efficiency.

4. Conclusions

After Papers I–V, in this study we estimate [Fe/H], age, distance, reddening and extinction of high-latitude low-extinction Galactic GCs NGC 5024 (M53), NGC 5053, NGC 5272 (M3), NGC 5466, and NGC 7099 (M30) by fitting BaSTI and DSED theoretical isochrones for $[\alpha/{\rm Fe}] = 0.4$ to CMDs based on multiband photometry. We employed the photometry in, at least, 25 filters from the HST, Gaia DR3, PS1, SDSS, SMSS DR3, UKIDSS, VISTA VHS DR5, unWISE, a large compilation of the *UBVRI* ground-based observations by SPZ19, and other data sets, most of which have never been fitted before. The filters under consideration span a wide wavelength range from the UV to mid-IR. HST and Gaia DR3 PMs and parallaxes are used to select the cluster members. Accordingly, we provided the median parallax and systemic PMs of the clusters. Cross-identification of the data sets allowed us to estimate systematic differences between them and verify that the CCM89 extinction law with $R_{\rm V} = 3.1$ is applicable to these clusters.

The obtained estimates of [Fe/H], age, distance, distance modulus, apparent *V*-band distance modulus, and reddening $E(B-V)$ for all the clusters are presented in Table 7. Our estimates of extinction are $A_{\rm V} = 0.08$, 0.06, 0.08, 0.08, and 0.16 mag for NGC 5024, NGC 5053, NGC 5272, NGC 5466, and NGC 7099, respectively, with statistical and systematic uncertainties of ± 0.01 and ± 0.03 mag respectively. Since three of four clusters near the North Galactic Pole demonstrate $A_{\rm V} = 0.08$, we suggested this value as the total Galactic extinction across the whole Galactic dust to extragalactic

[34] This includes all RR Lyrae variables of this cluster, as seen in Figures 2 and 6 (the RR Lyrae variables are eliminated in Figures 1, 3, and 4).

[35] Our minimum HB mass estimates by use of the best-fitting BaSTI isochrones almost coincide with those of Gratton et al. (2010), which are thus considered hereafter. The Gratton et al. (2010) estimates are based on an older model. Hence, this coincidence indicates that our conclusions about the HB morphology would be the same with any reliable HB model, not only with BaSTI.

[36] Much longer HB blue tail of NGC 6205, the famous HB second parameter mate of NGC 5272, can be explained by its even higher mass loss of 0.210 ± 0.020 and 0.273 ± 0.021 solar mass for two generations, respectively (Tailo et al. 2020).

[37] Yet another difference between the clusters is seen in Figure 2: NGC 5024 and NGC 5272 contain much more type II Cepheids, which populate the gap in the middle of the BaSTI AGB, i.e., the area III in Figure 6. Type II Cepheids are believed to be the immediate progeny of blue (i.e., low-mass) HB stars (Catelan 2009). Therefore, the lack of type II Cepheids in NGC 5053, NGC 5466, and NGC 7099 corresponds to the lack of the low-mass HB stars.

objects at the North polar cap. Our estimates of all the parameters agree with most estimates from the literature, while disapproving other estimates. In particular, our [Fe/H] estimates support lower [Fe/H] estimates from the literature for NGC 5272, while higher [Fe/H] estimates for the remaining low-metallicity clusters. Accordingly, our estimates support the arguments of Mucciarelli & Bonifacio (2020) in favor of photometrically and against spectroscopically derived [Fe/H] of clusters with [Fe/H] ≈ -2.

We recalculated the HB types of these clusters and analyzed the distribution of their HB stars with mass. This allowed us to explain their HB morphology difference by their different metallicity, age, mass-loss efficiency, and loss of low-mass members, including the bluest HB stars, in the dynamical evolution and mass segregation of core-collapse cluster NGC 7099 and loose clusters NGC 5053 and NGC 5466.

NGC 5024, NGC 5053, NGC 5466, and NGC 7099 have nearly the same metallicity, low helium enrichment, and age (NGC 5466 may be slightly younger), but only the former retains its low-mass stars. It is worth noting that our results on NGC 5024, NGC 5053, NGC 5466, and NGC 7099 do not contradict their captured origin from a satellite galaxy suggested by Yoon & Lee (2002).

Acknowledgments

We acknowledge financial support from the Russian Science Foundation (grant No. 20–72–10052).

We thank the anonymous reviewer for useful comments. We thank Armando Arellano Ferro for very fruitful discussion of the cluster RR Lyrae stars, Giacomo Beccari for providing of a data set with useful comments, Anupam Bhardwaj for providing a data set, Dong-Hwan Cho for providing a data set, Sang-Hyun Chun for providing a data set, Santi Cassisi for providing the valuable BaSTI isochrones with his exceptionally useful comments, Aaron Dotter for his comments on DSED, Heinz Frelijj for providing a data set, Gregory Green for discussion of extinction/reddening estimates in the fields of globular clusters, Frank Grundahl for providing his valuable Strömgren data sets with very useful comments, Young-Beom Jeon for providing a data set, K. J. Nikitha Jithendran for providing a data set, Christopher Onken, Taisia Rahmatulina and Sergey Antonov for their help to access the SkyMapper Southern Sky Survey DR3, Eric Sandquist for providing a data set with very useful discussion, Peter Stetson for providing and having discussion of his valuable *UBVRI* photometry, and Eugene Vasiliev for his very useful comments on the cluster properties.

This work has made use of BaSTI and DSED web tools; Filtergraph (Burger et al. 2013), an online data visualization tool developed at Vanderbilt University through the Vanderbilt Initiative in Data-intensive Astrophysics (VIDA) and the Frist Center for Autism and Innovation (FCAI, https://filtergraph.com); the resources of the Centre de Données astronomiques de Strasbourg, Strasbourg, France (http://cds.u-strasbg.fr), including the SIMBAD database, the VizieR catalog access tool (Ochsenbein et al. 2000) and the X-Match service; observations made with the NASA/ESA Hubble Space Telescope; data products from the Wide-field Infrared Survey Explorer, which is a joint project of the University of California, Los Angeles, and the Jet Propulsion Laboratory/California Institute of Technology; data products from the Pan-STARRS Surveys (PS1); data products from the Sloan Digital Sky Survey; data products from the SkyMapper Southern Sky Survey, SkyMapper is owned and operated by The Australian National University's Research School of Astronomy and Astrophysics, the SkyMapper survey data were processed and provided by the SkyMapper Team at ANU, the SkyMapper node of the All-Sky Virtual Observatory (ASVO) is hosted at the National Computational Infrastructure (NCI); data products from the Two Micron All Sky Survey, which is a joint project of the University of Massachusetts and the Infrared Processing and Analysis Center/California Institute of Technology, funded by the National Aeronautics and Space Administration and the National Science Foundation; data from the European Space Agency (ESA) mission Gaia (https://www.cosmos.esa.int/gaia), processed by the Gaia Data Processing and Analysis Consortium (DPAC, https://www.cosmos.esa.int/web/gaia/dpac/consortium), and Gaia archive website (https://archives.esac.esa.int/gaia).

Appendix
The Other Key CMDs of the Clusters

We present some other key CMDs of the clusters in Figures A1, A2, and A3.

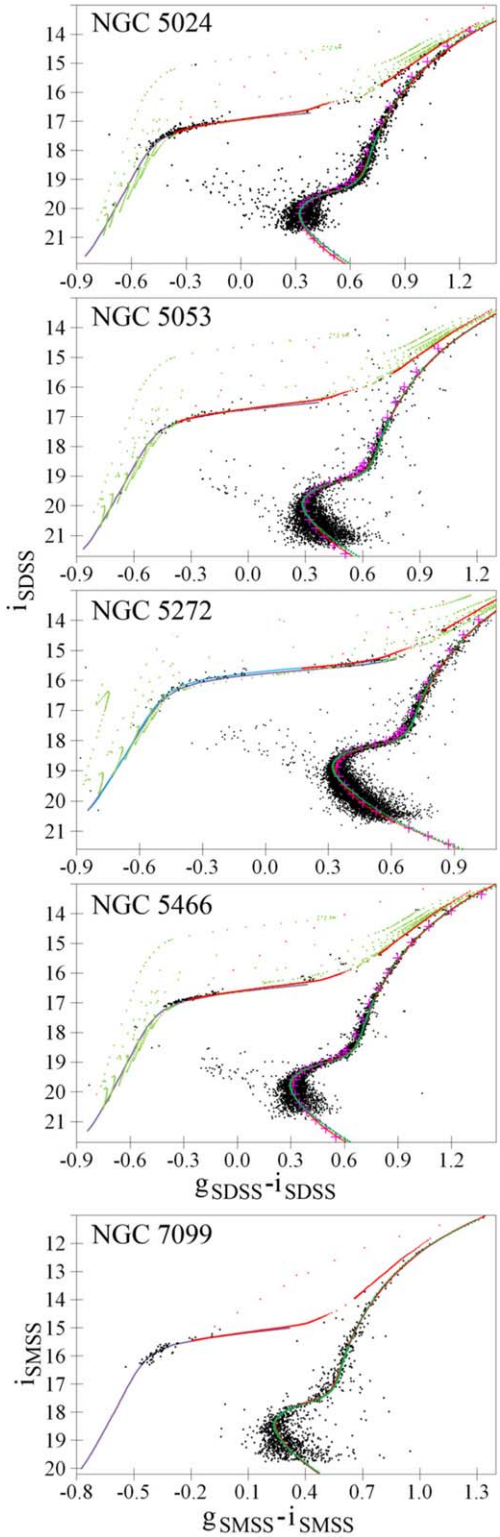

Figure A1. $g_{SDSS} - i_{SDSS}$ vs. i_{SDSS} CMDs for the Gaia cluster members from the SDSS data sets for NGC 5025, NGC 5272, NGC 5466 and all the stars from the initial SDSS data set for NGC 5053, as well as $g_{SMSS} - i_{SMSS}$ vs. i_{SMSS} CMD for the Gaia cluster members from the SMSS data set for NGC 7099. The fiducial sequences of An et al. (2008) are shown as the magenta crosses. The isochrones for $Y = 0.25$ from BaSTI (red), DSED (green), BaSTI ZAHB (purple), DSED HB/AGB (light green), as well as the NGC 5272 BaSTI ZAHB for $Y = 0.275$ (blue) are calculated with the best-fitting parameters from Table 6. RR Lyrae variables are eliminated, except the plot for NGC 5053.

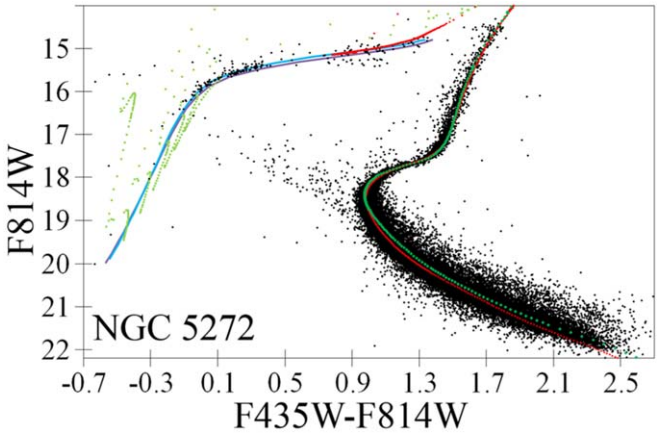

Figure A2. HST/ACS F435W–F814W vs. F814W CMD for the NGC 5272 Libralato et al. (2022) data set. The isochrones for $Y = 0.25$ from BaSTI (red), DSED (green), BaSTI ZAHB (purple), and DSED HB/AGB (light green) are calculated with the best-fitting parameters from Table 6. RR Lyrae variables are retained.

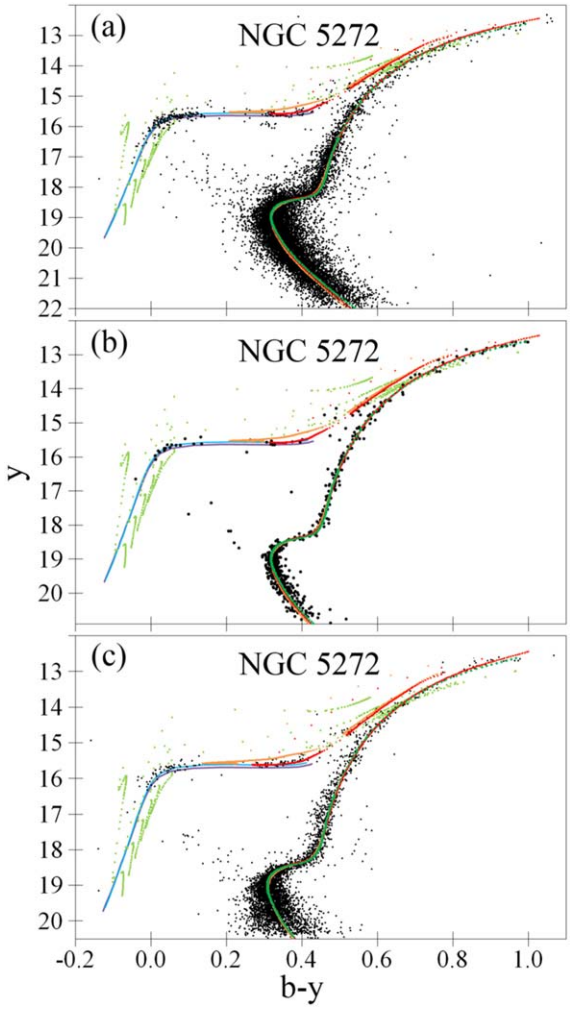

Figure A3. Strömgren $b - y$ vs. y CMDs for NGC 5272: (a) all the stars from the GCL99 data set, (b) the Gaia cluster members from the GCL99 data set, (c) the Gaia cluster members from the Massari et al. (2016) data set. The isochrones for $Y = 0.25$ from BaSTI (red), DSED (green), BaSTI ZAHB (purple), DSED HB/AGB (light green), as well as for $Y = 0.275$ from BaSTI (orange) and BaSTI ZAHB (blue) are calculated with the best-fitting parameters from Table 6. RR Lyrae variables are retained in the plot (a), while eliminated in the plots (b) and (c).

References

An, D., Johnson, J. A., Clem, J. L., et al. 2008, ApJS, 179, 326
An, D., Pinsonneault, M. H., Masseron, T., et al. 2009, ApJ, 700, 523
Anderson, J., Sarajedini, A., Bedin, L. R., et al. 2008, AJ, 135, 2055
Arellano Ferro, A. 2022, RMxAA, 58, 257
Arellano Ferro, A. 2024, in IAU Symp. 376, At the Crossroads of Astrophysics and Cosmology: Period-luminosity Relations in the 2020s, ed. R. de Grijs, P. A. Whitelock, & M. Catelan (Cambridge: Cambridge Univ. Press), 222
Arellano Ferro, A., Giridhar, S., & Bramich, D. M. 2010, MNRAS, 402, 226
Baumgardt, H., & Vasiliev, E. 2021, MNRAS, 505, 5957
Beccari, G., Dalessandro, E., Lanzoni, B., et al. 2015, ApJ, 814, 144
Beccari, G., Dalessandro, E., Lanzoni, B., et al. 2013, ApJ, 776, 60
Bernard, E. J., Ferguson, A. M. N., Schlafly, E. F., et al. 2014, MNRAS, 442, 2999
Bica, E., Pavani, D. B., Bonatto, C. J., & Lima, E. F. 2019, AJ, 157, 12
Boberg, O. M., Friel, E. D., & Vesperini, E. 2015, ApJ, 804, 109
Boberg, O. M., Friel, E. D., & Vesperini, E. 2016, ApJ, 824, 5
Bonatto, C., Campos, F., & Kepler, S. O. 2013, MNRAS, 435, 263
Buonanno, R., Corsi, C. E., Buzzoni, A., et al. 1994, A&A, 290, 69
Burger, D., Stassun, K. G., Pepper, J., et al. 2013, A&C, 2, 40
Cardelli, J. A., Clayton, G. C., & Mathis, J. S. 1989, ApJ, 345, 245
Carretta, E., Bragaglia, A., Gratton, R., D'Orazi, V., & Lucatello, S. 2009, A&A, 508, 695
Carretta, E., Bragaglia, A., Gratton, R. G., et al. 2010, A&A, 516, A55
Casagrande, L., & VandenBerg, D. A. 2014, MNRAS, 444, 392
Casagrande, L., & VandenBerg, D. A. 2018a, MNRAS, 479, L102
Casagrande, L., & VandenBerg, D. A. 2018b, MNRAS, 475, 5023
Catelan, M. 2009, Ap&SS, 320, 261
Chambers, K. C., Magnier, E. A., Metcalfe, N., et al. 2016, arXiv:1612.05560
Chun, S.-H., Lee, J.-J., & Lim, D. 2020, ApJ, 900, 146
Chun, S.-H., Kim, J.-W., Sohn, S. T., et al. 2010, AJ, 139, 606
Cohen, R. E., Hempel, M., Mauro, F., et al. 2015, AJ, 150, 176
Dalessandro, E., Salaris, M., Ferraro, F. R., Mucciarelli, A., & Cassisi, S. 2013, MNRAS, 430, 459
Denissenkov, P. A., VandenBerg, D. A., Kopacki, G., & Ferguson, J. W. 2017, ApJ, 849, 159
Dotter, A., Chaboyer, B., Jevremović, D., et al. 2007, AJ, 134, 376
Dotter, A., Chaboyer, B., Jevremović, D., et al. 2008, ApJS, 178, 89
Dotter, A., Sarajedini, A., Anderson, J., et al. 2010, ApJ, 708, 698
Eisenstein, D. J., Liebert, J., Harris, H. C., et al. 2006, ApJS, 167, 40
Fekadu, N., Sandquist, E. L., & Bolte, M. 2007, ApJ, 663, 277
Forbes, D. A., & Bridges, T. 2010, MNRAS, 404, 1203
Gaia Collaboration, Vallenari, A., Brown, A. G. A., et al. 2023, A&A, 674, A1
Goldsbury, R., Richer, H. B., Anderson, J., et al. 2010, AJ, 140, 1830
Gontcharov, G. A., Khovritchev, M. Y., & Mosenkov, A. V. 2020, MNRAS, 497, 3674
Gontcharov, G. A., Marchuk, A. A., Khovrichev, M. Y., et al. 2023a, AstL, 49, 673
Gontcharov, G. A., Khovritchev, M. Y., Mosenkov, A. V., et al. 2023b, MNRAS, 518, 3036
Gontcharov, G. A., Bonatto, C. J., Ryutina, O. S., et al. 2023c, MNRAS, 526, 5628
Gontcharov, G. A., Mosenkov, A. V., & Khovritchev, M. Y. 2019, MNRAS, 483, 4949
Gontcharov, G. A., Khovritchev, M. Y., Mosenkov, A. V., et al. 2021, MNRAS, 508, 2688
Gratton, R. G., Carretta, E., Bragaglia, A., Lucatello, S., & D'Orazi, V. 2010, A&A, 517, A81
Green, G. M., Schlafly, E., Zucker, C., Speagle, J. S., & Finkbeiner, D. 2019, ApJ, 887, 93
Grundahl, F., Catelan, M., Landsman, W. B., Stetson, P. B., & Andersen, M. I. 1999, ApJ, 524, 242
Harris, W. E. 1996, AJ, 112, 1487
Hewett, P. C., Warren, S. J., Leggett, S. K., & Hodgkin, S. T. 2006, MNRAS, 367, 454
Hidalgo, S. L., Pietrinferni, A., Cassisi, S., et al. 2018, ApJ, 856, 125
Hunt, E. L., & Reffert, S. 2023, A&A, 673, A114
Jeon, Y.-B., Lee, M. G., Kim, S.-L., & Lee, H. 2004, AJ, 128, 287
Jurcsik, J., & Hajdu, G. 2023, MNRAS, 525, 3486
Kacharov, N., Koch, A., Caffau, E., & Sbordone, L. 2015, A&A, 577, A18
Kains, N., Bramich, D. M., Arellano Ferro, A., et al. 2013, A&A, 555, A36
Kimmig, B., Seth, A., Ivans, I. I., et al. 2015, AJ, 149, 53
Lallement, R., Babusiaux, C., Vergely, J. L., et al. 2019, A&A, 625, A135
Lauchner, A., Powell, W., Lee, J., & Wilhelm, R. 2006, ApJL, 651, L33
Lee, Y.-W., Demarque, P., & Zinn, R. 1994, ApJ, 423, 248
Libralato, M., Bellini, A., Vesperini, E., et al. 2022, ApJ, 934, 150
Lindegren, L., Bastian, U., Biermann, M., et al. 2021, A&A, 649, A4
Mansfield, S., Dieball, A., Kroupa, P., et al. 2022, MNRAS, 511, 3785
Massari, D., Lapenna, E., Bragaglia, A., et al. 2016, MNRAS, 458, 4162
Masseron, T., García-Hernández, D. A., Mészáros, S., et al. 2019, A&A, 622, A191
McMahon, R. G., Banerji, M., Gonzalez, E., et al. 2013, Msngr, 154, 35
Meisner, A. M., & Finkbeiner, D. P. 2015, ApJ, 798, 88
Mészáros, S., Masseron, T., García-Hernández, D. A., et al. 2020, MNRAS, 492, 1641
Meylan, G., & Heggie, D. C. 1997, A&Ar, 8, 1
Milone, A. P., Piotto, G., Renzini, A., et al. 2017, MNRAS, 464, 3636
Milone, A. P., Marino, A. F., Renzini, A., et al. 2018, MNRAS, 481, 5098
Mucciarelli, A., & Bonifacio, P. 2020, A&A, 640, A87
Mucciarelli, A., Lovisi, L., Lanzoni, B., & Ferraro, F. R. 2014, ApJ, 786, 14
Nardiello, D., Libralato, M., Piotto, G., et al. 2018, MNRAS, 481, 3382
Nikitha, K. J., Vig, S., & Ghosh, S. K. 2022, MNRAS, 514, 5570
Ochsenbein, F., Bauer, P., & Marcout, J. 2000, A&AS, 143, 23
Odenkirchen, M., & Grebel, E. K. 2004, in ASP Conf. Ser. 327, Satellites and Tidal Streams, ed. F. Prada, D. Martinez Delgado, & T. J. Mahoney (San Francisco, CA: ASP), 284
Onken, C. A., Wolf, C., Bessell, M. S., et al. 2019, PASA, 36, e033
Paust, N. E. Q., Reid, I. N., Piotto, G., et al. 2010, AJ, 139, 476
Pietrinferni, A., Hidalgo, S., Cassisi, S., et al. 2021, ApJ, 908, 102
Piotto, G., King, I. R., Djorgovski, S. G., et al. 2002, A&A, 391, 945
Piotto, G., Milone, A. P., Bedin, L. R., et al. 2015, AJ, 149, 91
Preet Kaur, K., & Joshi, P. S. 2022, arXiv:2209.03019
Reimers, D. 1975, MSRSL, 8, 369
Rey, S.-C., Lee, Y.-W., Byun, Y.-I., & Chun, M.-S. 1998, AJ, 116, 1775
Rey, S.-C., Yoon, S.-J., Lee, Y.-W., Chaboyer, B., & Sarajedini, A. 2001, AJ, 122, 3219
Riello, M., De Angeli, F., Evans, D. W., et al. 2021, A&A, 649, A3
Sandage, A. R. 1953, AJ, 58, 61
Sandquist, E. L., Bolte, M., Langer, G. E., Hesser, J. E., & de Oliveira, C. M. 1999, ApJ, 518, 262
Sarajedini, A., & Milone, A. A. E. 1995, AJ, 109, 269
Schlafly, E. F., & Finkbeiner, D. P. 2011, ApJ, 737, 103
Schlafly, E. F., Meisner, A. M., & Green, G. M. 2019, ApJS, 240, 30
Schlegel, D. J., Finkbeiner, D. P., & Davis, M. 1998, ApJ, 500, 525
Simioni, M., Bedin, L. R., Aparicio, A., et al. 2018, MNRAS, 476, 271
Skrutskie, M. F., Cutri, R. M., Stiening, R., et al. 2006, AJ, 131, 1163
Sollima, A., Dalessandro, E., Beccari, G., & Pallanca, C. 2017, MNRAS, 464, 3871
Stenning, D. C., Wagner-Kaiser, R., Robinson, E., et al. 2016, ApJ, 826, 41
Stetson, P. B., Pancino, E., Zocchi, A., Sanna, N., & Monelli, M. 2019, MNRAS, 485, 3042
Tailo, M., Milone, A. P., Lagioia, E. P., et al. 2020, MNRAS, 498, 5745
Torelli, M., Iannicola, G., Stetson, P. B., et al. 2019, A&A, 629, A53
Valcarce, A. A. R., Catelan, M., Alonso-García, J., Contreras Ramos, R., & Alves, S. 2016, A&A, 589, A126
Valcin, D., Bernal, J. L., Jimenez, R., Verde, L., & Wandelt, B. D. 2020, JCAP, 2020, 002
VandenBerg, D. A., Brogaard, K., Leaman, R., & Casagrande, L. 2013, ApJ, 775, 134
Vasiliev, E., & Baumgardt, H. 2021, MNRAS, 505, 5978
Vitral, E. 2021, MNRAS, 504, 1355
Wright, E. L., Eisenhardt, P. R. M., Mainzer, A. K., et al. 2010, AJ, 140, 1868
Yang, Y., Zhao, J.-K., Tang, X.-Z., Ye, X.-H., & Zhao, G. 2023, ApJ, 953, 130
Yoon, S.-J., & Lee, Y.-W. 2002, Science, 297, 578